Andean structural control on interseismic coupling in the North Chile subduction zone

Marta Béjar-Pizarro[1,2], Anne Socquet[3], Rolando Armijo[1], Daniel Carrizo[4], Jeff Genrich[5], Mark Simons[5]

[1] Institut de Physique du Globe de Paris, Sorbonne Paris Cité, Univ Paris Diderot, UMR 7154 CNRS, F-75005 Paris, France.

[2] InSARlab Geohazards InSAR laboratory, Geoscience Research dept., Geological Survey of Spain, Alenza 1, 28003, Spain.

[3] Université Joseph Fourier - Grenoble I, OSUG - Observatoire des Sciences de l'Univers de Grenoble, ISTerre - Institut des Sciences de la Terre Maison des Géosciences 1381, rue de la Piscine 38400 - Saint Martin d'Heres, France.

[4] Departamento de Geofísica, Facultad de Ciencias Físicas y Matemáticas, Universidad de Chile, Blanco Encalada 2002, Santiago, Chile.

[5] Seismological Laboratory, Division of Geological and Planetary Sciences, California Institute of Technology, Pasadena, CA 91125, USA.

Contents:

1 GPS velocity estimation

We estimate interseismic velocities in 29 GPS stations (Fig.1 and Fig.S1) of the CAnTO (Caltech Andes Tectonic Observatory) and LIA Montessus de Ballore (Universidad de Chile, CNRS INSU, Institut de Recherche pour le Développement) continuous GPS Networks. These networks record daily positions estimates, with time series durations up to 10 years. Here we present the first interseismic velocities measured by these permanent networks.

We use GAMIT software (King and Bock, 2002) to reduce 24-h sessions to daily estimates of station positions, using the ionosphere free L3 observable and fixing ambiguities to integer values when possible. The daily solutions are then combined into time series, using the GLRED software (Herring, 2002).

We determine the GPS velocity field in North Chile using these time series for the period 2003-2009 (Fig. S1). For each component of the time series, we filter data corresponding to the dates of two earthquakes that occurred in the region during the period analysed (13/06/2005 Mw 7.7 Tarapacá and 14/11/2007 Mw 7.7 Tocopilla earthquake) plus two months after each earthquake (to eliminate the potential postseismic deformation). Then we fit an equation comprising a linear trend (velocity component), a seasonal periodic signal and a Heaviside step function:

$$y(t_i) = \ a + bt_i + \sum_{j=1}^{n} c_j H(t_i - T_j) + d\sin(2\pi t_i) + e\cos(2\pi t_i) + f\sin(4\pi t_i) + g\cos(4\pi t_i) \qquad (1)$$

where ti is time in seconds, b is the constant interseismic velocity of the station and H denotes the Heaviside unit step function used to correct position offsets at the time T_j, introduced by antenna changes and coseismic signals of the two earthquakes. Coefficients d and e refer to an annual signal and f, g, describe a semi-annual signal. These periodic terms are used to account for the seasonal variations in site positions from various sources (e.g. surface mass redistribution, unmodeled wet troposphere effects, bedrock thermal expansion, (e.g., Dong et al., 2002). Examples of two time series are shown in Figs S2 and S3.

This procedure leads to horizontal and vertical velocities with respect to the International Terrestrial Reference Frame (ITRF) 2005 (Altamimi et al., 2007). Following Mao et al. (1999) we model the noise associated with our time series as a combination of white noise and coloured noise (here random-walk noise). For each time series, the mean residual between the data and the fit equation is calculated. We estimate the size of both the random-walk and the white noise components by fitting a curve to the power spectrum of the residuals (e.g., Langbein and Johnson, 1997). These values are used to calculate the uncertainties associated with our velocity estimate. The 29 velocities present mean uncertainties in the east, north and vertical components of 1.6 mm/yr, 1.3 mm/yr and 3.0 mm/yr. Station positions, velocities, time series mean RMS and velocity uncertainties appear in Table S1.

We compute velocities relative to the South-American plate by applying the rigid rotation of South-America in ITRF2005 plate model (16.800°S, 129.631°W, 0.121°/Ma, Altamimi et al., 2007) to our data set in the ITRF. The estimated horizontal velocity field (Fig. 1) is characterized by vectors subparallel to Nazca-South America convergence, with a magnitude decreasing away from the trench. This indicates that the upper plate is compressed by interseismic loading. The vertical velocity field shows uplift almost everywhere implying that coupling cannot extend far under the continent.

2 InSAR velocity estimation

We use SAR interferometry (InSAR) to measure ground motion in the satellite line of sight (LOS). We processed Envisat ASAR (5.6 cm wavelength) data acquired with a descending track (t96, satellite moving south and looking down to the west). Data were acquired between 2003 and 2009 and they present varying sizes in latitude (Figure S4).

To avoid contamination of the interseismic signal from coseismic signals of the 2005 Tarapacá and 2007 Tocopilla earthquakes (figure S4(b)), we studied separately the region affected by the 2005 Tarapacá earthquake (north of latitude -21.5° in our InSAR data, hereafter referred as the northern region) and the region affected by the 2007 Tocopilla earthquake (south of latitude -21.5° in our InSAR data, hereafter referred as the southern region). Figure S5 is a baseline/time plot showing how ASAR images were combined to obtain both stacks.

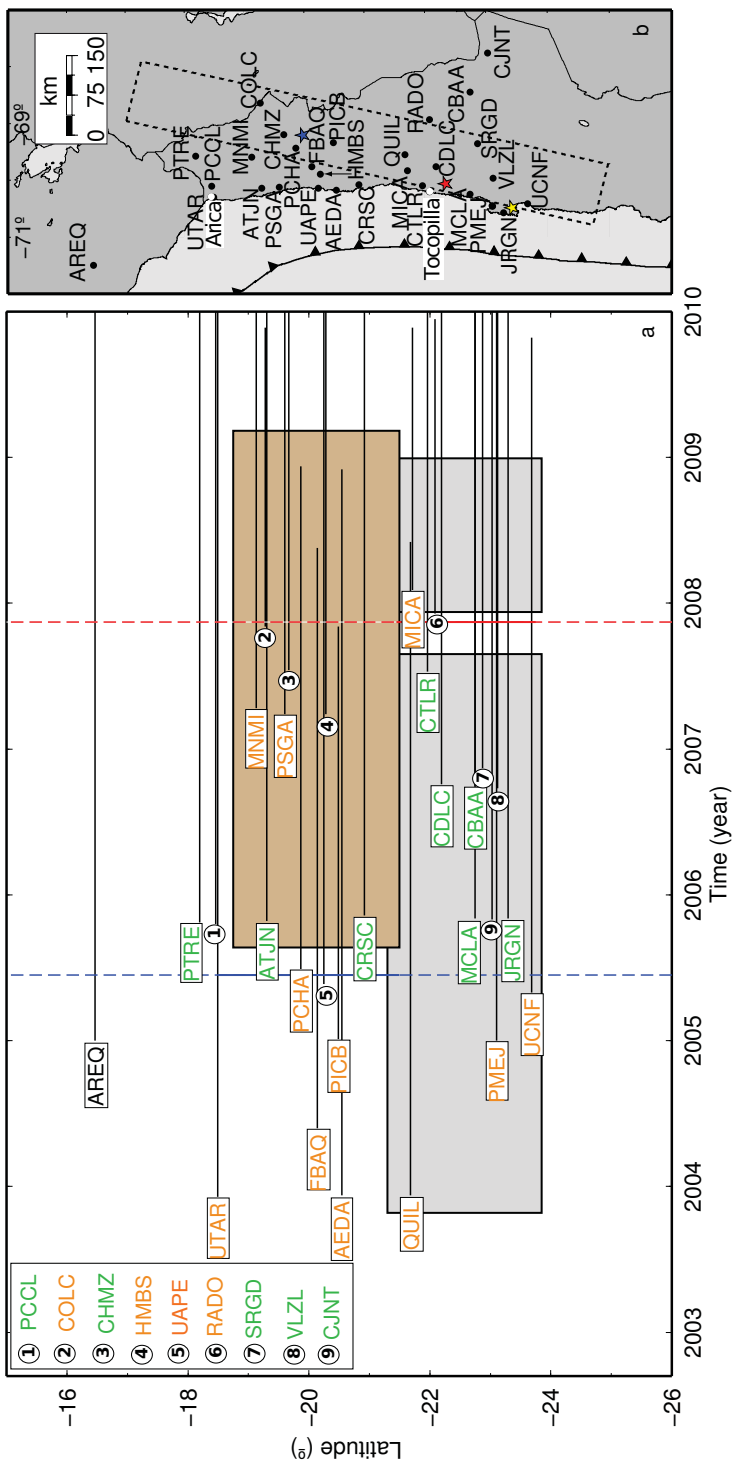

Figure S1: Spatial and temporal extent of GPS data used in this study. (a) Horizontal black lines represent time series for each station (name indicated on the left side box in each line) showing its position in latitude and its total time span. Names of GPS sites are coloured to indicate the network to which they belong: green for CAnTO GPS Network, orange for LIA Montessus de Ballore Network and black indicates IGS Network. Brown and gray rectangular areas represent the time interval and latitudinal extent of the north and south InSAR stacks respectively. The two vertical dashed lines represent the date of the 2005 Tarapacá (blue line) and the 2007 Tocopilla (red line) earthquakes. (b) Black dots show locations of GPS stations and the dashed black rectangle delimits the approximate extents of our SAR data. Stars indicate epicentres of the Mw 8.1 Antofagasta, Mw 7.7 Tarapacá and Mw 7.7 Tocopilla earthquakes (yellow, blue and red respectively).

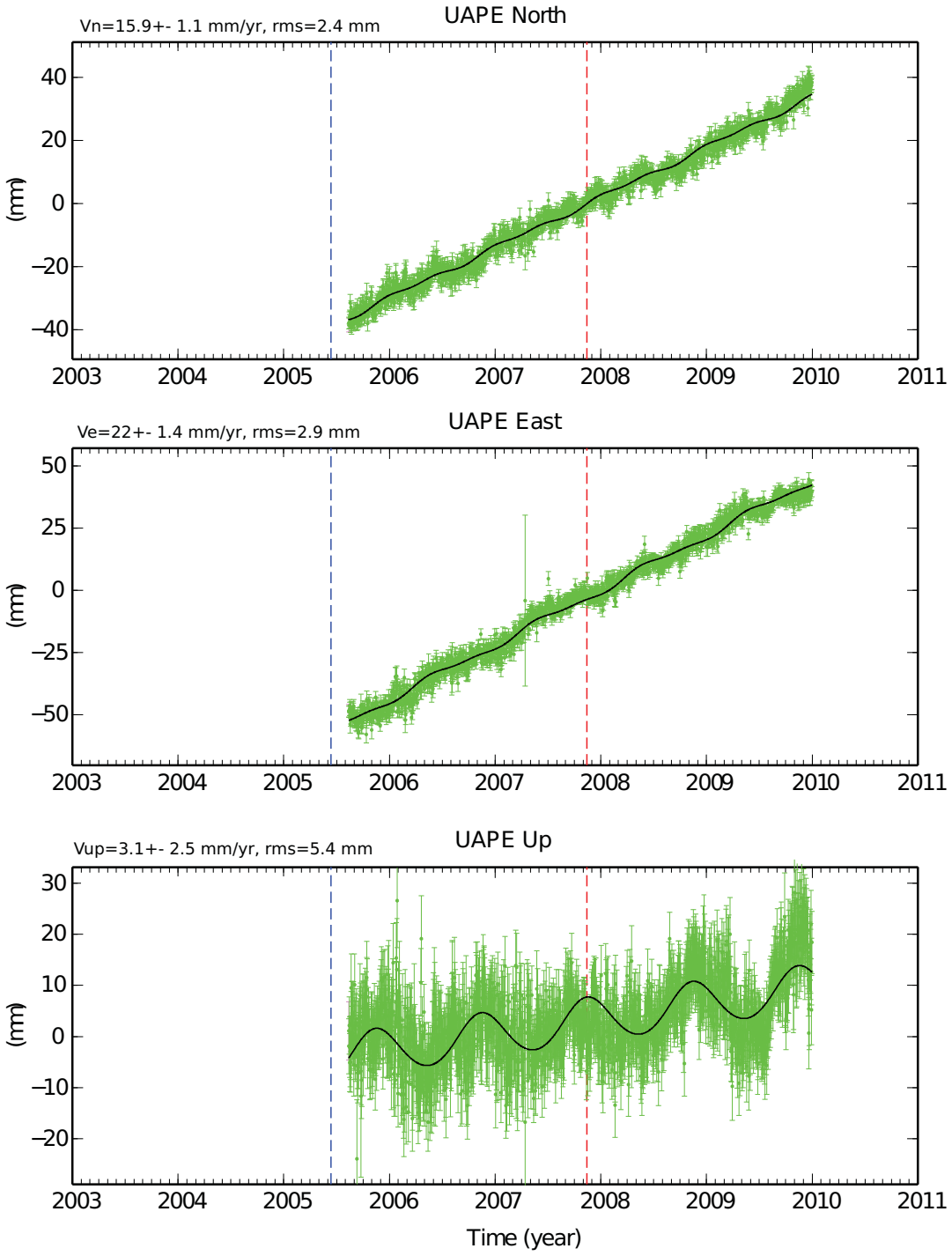

Figure S2: North, East and Vertical GPS time series of displacements recorded at UAPE station. Green points show the recorded positions with respect to the ITRF2005, with 2σ uncertainties. The black curve represents the modeled displacements (using equation 1). Vertical dashed lines represent the date of the 13/06/2005 Tarapacá (blue line) and 14/11/2007 Tocopilla (red line) earthquakes. Resulting velocities and rms for each component are indicated on the upper left of each graphic.

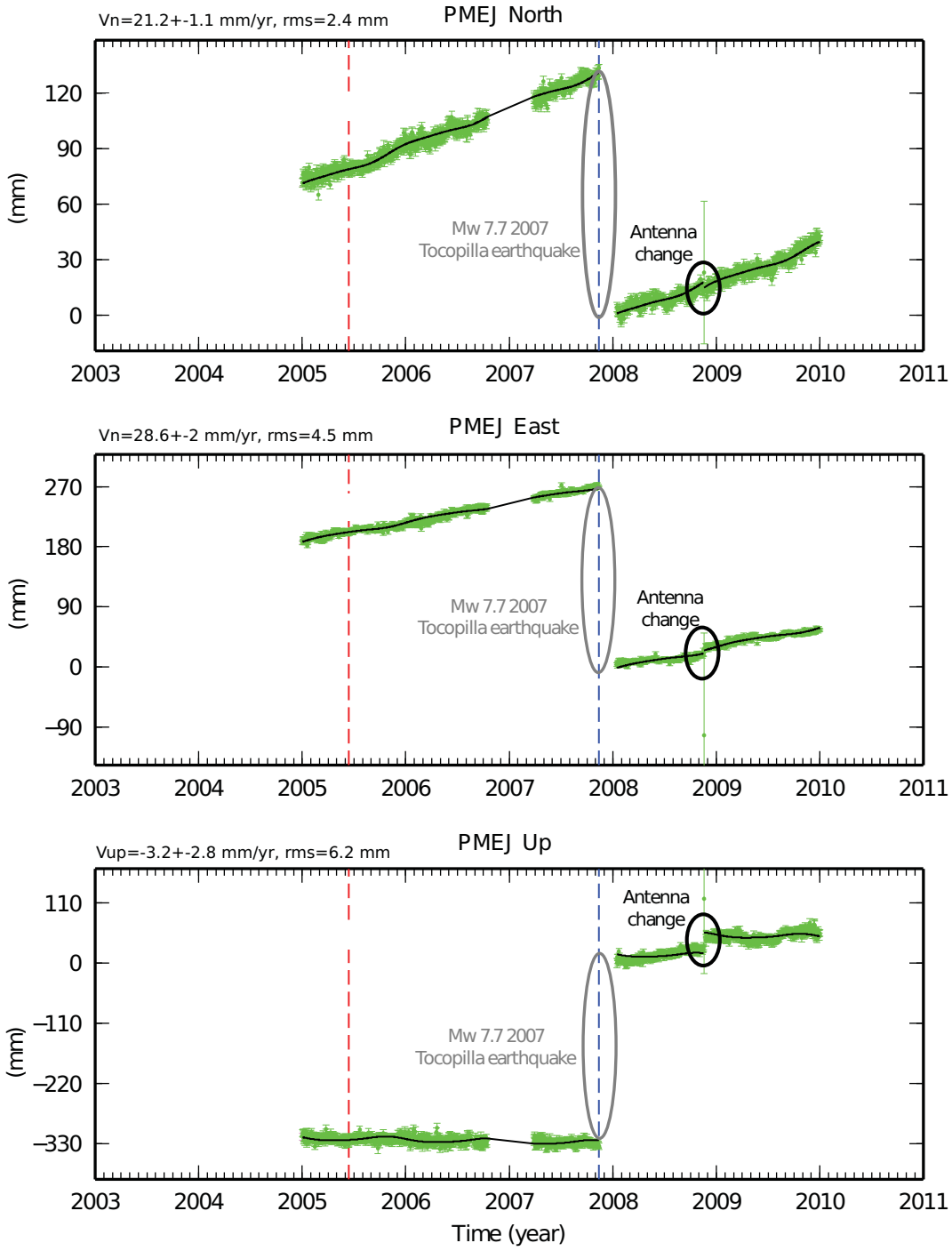

Figure S3: North, East and Vertical GPS time series of displacements recorded at PMEJ station. Conventions are the same as in Fig. S2. Offsets introduced by the coseismic signal of the 2007 Tocopilla earthquake and an antenna change in 2008 (gray and black ellipses, respectively) have been corrected with the Heaviside step function.

SITE	Lon	Lat	Ve (itrf)	Vn (itrf)	Vup (itrf)	s Ve	s Vn	s Vup	Ve (soam)	Vn(soam)
MCLA[a]	-70.248	-22.746	25.7±1.6	19.3±1.2	4±2.3	3.2	2.4	4.6	26.8	8.2
CTLR[a]	-70.097	-21.964	26.1±1.4	20±1.5	4.3±2.6	2.2	2.3	4.0	27.3	8.9
VLZL[a]	-69.96	-23.12	21.8±1.7	18.7±1.3	6.1±3.1	3.1	2.3	5.5	22.8	7.6
SRGD[a]	-69.35	-22.87	15.8±1.8	16.9±1.3	0±3.2	3.1	2.3	5.6	16.9	5.7
PCCL[a]	-70.107	-18.458	14.6±1.4	16.1±1.1	2.3±2.4	2.8	2.3	5.0	16.2	5.0
JRGN[a]	-70.575	-23.289	28.5±1.7	20.9±1.3	2.7±2.6	3.5	2.6	5.2	29.5	9.9
CJNT[a]	-67.761	-23.027	12.6±1.5	16.8±1.2	3.3±2.3	3.1	2.5	4.6	13.8	5.4
CBAA[a]	-68.448	-22.746	10.9±1.7	16.9±1.3	2.9±2.6	3.1	2.3	4.6	12.1	5.6
CDLC[a]	-69.76	-22.19	23.5±1.5	17.2±1.3	3.9±2.6	2.7	2.4	4.6	24.7	6.1
CRSC[a]	-70.08	-20.92	26±1.3	19±1.1	4.8±2.3	2.7	2.3	4.6	27.3	7.9
CHMZ[a]	-69.194	-19.669	16.8±1.6	16.2±1.7	3.5±2.7	2.5	2.6	4.2	18.3	5.0
ATJN[a]	-70.137	-19.301	20.1±1.6	16±1.2	4±2.4	3.3	2.4	4.8	21.6	4.9
PTRE[a]	-69.575	-18.195	9.2±1.3	17.9±1.1	0.4±2.4	2.7	2.3	4.9	10.9	6.7
PMEJ[b]	-70.448	-23.101	28.6±2	21.2±1.1	-3.2±2.8	4.5	2.4	6.2	29.6	10.1
UCNF[b]	-70.41	-23.68	29.4±1.2	18.3±1.1	2.7±2	2.5	2.3	4.3	30.3	7.2
RADO[b]	-68.927	-22.083	12.8±1.6	15.2±1.6	-2.6±3	2.3	2.3	4.2	14.0	4.0
UAPE[b]	-70.141	-20.243	22±1.4	15.9±1.1	3.1±2.5	2.9	2.4	5.4	23.4	4.8
HMBS[b]	-69.888	-20.278	13.4±2.4	13.6±1.5	0±3.6	4.0	2.5	6.0	14.8	2.5
PICB[b]	-69.335	-20.49	20.3±2.3	15.1±1.4	3.4±4.3	3.9	2.4	7.3	21.7	3.9
PCHA[b]	-69.432	-19.869	17.8±1.6	15.6±1.5	2.7±3	3.0	2.7	5.5	19.3	4.4
PSGA[b]	-70.123	-19.597	19.5±1.9	16.3±1.4	-0.1±3	3.1	2.4	4.9	21.0	5.2
MNMI[b]	-69.596	-19.131	12.6±1.5	17.8±1.4	1.4±2.7	2.5	2.3	4.5	14.2	6.6
COLC[b]	-68.639	-19.276	12.4±1.8	16.1±1.5	-0.6±3.9	2.6	2.2	5.6	14.0	4.8
UTAR[b]	-70.297	-18.491	15.6±1.1	15±0.9	3.7±3.4	2.5	1.9	7.5	17.2	3.9
MICA[b]	-69.827	-21.715	25.6±1.6	17.7±1.6	5.6±3.1	2.2	2.2	4.1	26.8	6.6
AEDA[b]	-70.178	-20.546	24±1.8	16.9±1.2	0.4±4.9	2.5	1.7	6.9	25.3	5.8
QUIL[b]	-69.55	-21.68	27.3±1.8	17.2±1.2	1.8±4.5	2.1	1.4	5.2	28.5	6.0
FBAQ[b]	-69.756	-20.135	20±1.5	16.5±1.4	9.8±5	2.1	2.0	7.0	21.4	5.4
AREQ[c]	-71.493	-16.465	-1.4±1.4	8.1±1.2	3±2.4	3.2	2.7	5.3	0.4	-2.8

Table S1: Velocity vectors used in this study, estimated from GPS time series using equation 1. Our final velocity field has been obtained by a combination of independent processing of two subsets of stations. Both processing were performed using the Gamit GlobK software, and projected into ITRF2005. Stations MCLA, CTLR, VLZL, SRGD, PCCL, JRGN, CJNT, CBAA, CDLC, CRSC, CHMZ, ATJN, PTRE, UCNF, UAPE, PCHA ,PSGA, COLC, AREQ were processed in Caltech while stations PMEJ, RADO, HMBS, PICB, MNMI, UTRA, MICA, AEDA, QUIL, FBAQ were processed in IPGP. Column 1 shows site name and GPS network ([a] refers to CAnTO GPS Network,[b] indicates LIA Montessus de Ballore Network and [c] indicates IGS Network). Columns 2 and 3 show location of GPS sites (in °), columns 4, 5 and 6 show velocities with respect to the ITRF2005 with their associated uncertainties. Columns 7, 8 and 9 contain RMS of the residual between the data and the fit equation. Columns 10 and 11 show velocities estimated with respect to South America. All velocities and associated uncertainties are in mm/yr, RMS values are in mm.

Data were processed using the Caltech/JPL repeat-orbit interferometry package, ROI PAC (Rosen et al., 2004). We construct each interferogram by calculating the phase difference between two ASAR images using the 2-pass approach (see Massonnet and Feigl, 1998, for an overview of the method). The topographic phase contribution was removed using a 3-arc-sec (90-m) digital elevation model from the Shuttle Radar Topography Mission (SRTM) (Farr and Kobrick, 2000). The orbital information used in the processing was provided by the European Space Agency (DORIS orbits).

Interferograms contain the relative displacement between the two dates in the radar LOS direction from ground to satellite, which is inclined ~ 23 ° from the vertical, varying from 18 ° in the near range to 26 ° in the far range. Therefore they are mostly sensitive to vertical displacements. The coherence in the interferograms is generally good, except in regions of high relief (northern part of the interferograms) where some interferograms present coherence loss.

The main difficulty to extract interseismic deformation in our InSAR data is due to the similarity between the long-wavelength topographic signal and the interseismic deformation signal (see for example Fig. S6). The small amplitude deformation is combined in the satellite LOS with orbital errors and atmospheric phase delays of similar or even larger amplitude. The important variations in elevation across our interferograms (from sea level to more than 5000 m in the Andes) are associated with significant variations in the troposphere water vapour content, that induce propagation delays correlated with topography in our interferograms (Doin et al., 2009; Hanssen, 2001; Remy et al., 2011; Fournier et al., 2011).

To retrieve the tectonic signal from InSAR data, we simultaneously correct orbital and atmospheric errors in individual interferograms and then we stack them to obtain an average velocity map. Orbital errors are corrected by removing a best-fit linear polynomial ramp from interferograms, using GPS velocities as a reference. We project GPS observations in the LOS direction and compare them with InSAR data at same locations. We use 4 GPS stations to correct the orbital ramp in the northern region and 10 GPS stations to estimate the orbital ramp in the southern region (see LOS differences between GPS velocities and LOS velocities in the final stack in Table S3). Errors associated with the phase delay through the troposphere are corrected by estimating the delay to elevation relationship observed in interferograms. In order to only eliminate the part of the signal related to the small wavelength topography, we estimate the phase/elevation relationship in small windows (10 x 10 km) throughout each complete interferogram. We obtain a value of the slope phase / elevation in each window, as shown in Fig. S7(c). To reduce the local variability in the phase/topography slope values, we fit a 3 degree polynomial function of elevation. The corrected interferograms are then stacked together to form an average velocity map for the southern (Fig. S9) and for the northern region (Fig. S10).

In order to evaluate the effectiveness of the corrections applied to interferograms, we have compared in Table S2 the rms of the slopes (phase/elevation) in each interferogram before and after the correction, in the final stack and in the deformation field predicted by a forward model (with coupling parallel to the coast, model D in Fig. S14). Figure S8 compares graphically both, the slope/elevation and the phase/elevation relationship for one interferogram, the final stack and the synthetic interferogram predicted by model D. Although the tectonic model is correlated with the long wavelength topography (i.e., the phase/topography plot is not centred to 0 but instead exhibits a small negative value), our correction method efficiently reduces the tropospheric delays by capturing the small wavelength correlation without removing the long wavelength tectonic signal. Indeed, values of the phase/elevation slope in the stack are significantly reduced, centred around zero, and comparable to values present in a forward model (which only contains tectonic deformation), suggesting that atmosphere contribution has been successfully removed from interferograms.

Figure S11 summarizes geodetic velocities estimated in this work. The InSAR deformation field is

Interferogram	original	corrected	Stack	Model
030922-071105^S	5.61	0.63		
031027-070827^S	4.95	0.55		
031201-070129^S	4.86	0.72		
040209-070409^S	9.20	0.64		
040315-051031^S	6.49	1.15		
040419-060703^S	6.51	0.70	Stack South	Model South
040524-050926^S	3.69	1.59	0.65	0.34
050718-060807^S	2.11	1.50		
071210-081229^S	2.96	1.48		
080114-090727^S	9.65	1.45		
080218-090309^S	3.35	1.60		
080428-090831^S	2.33	1.03		
050718-060807^N	1.72	1.31		
050822-080811^N	1.44	0.44		
060213-090727^N	9.37	0.63	Stack North	Model North
070129-090309^N	3.68	0.89	0.45	0.42
070305-090831^N	4.62	0.81		
070409-080707^N	1.79	0.93		

Table S2: Values of the root mean square (rms) of the slopes phase/elevation estimated in individual interferograms, the final stack and one of the forward models. Column 1 identifies each interferogram (date of each image has format yymmdd), columns 2 and 3 show rms values for each interferogram, before (original) and after correction (corrected). ^{S} indicates interferograms used in the stack for the southern region and ^{N} indicates interferograms used in the stack for the northern region. Column 4 contains rms values for the southern and northern stack. Column 5 contains rms values estimated in the deformation field predicted by a forward model where the base of the coupled region is parallel to the coastline (model D, Fig. S14). All rms values are in rad/km.

Site	Lon	Lat	diff-LOS	rms
CDLC^S	-69.76	-22.19	-2.07	
MCLA^S	-70.25	-22.75	1.24	
SRGD^S	-69.35	-22.87	-0.99	
VLZL^S	-69.96	-23.12	2.04	
CTLR^S	-70.10	-21.96	-0.31	2.53
MICA^S	-69.83	-21.71	0.34	
QUIL^S	-69.55	-21.68	3.82	
RADO^S	-68.93	-22.08	3.98	
PMEJ^S	-70.45	-23.10	-3.35	
UCNF^S	-70.41	-23.68	-3.35	
PCHA^N	-69.43	-19.87	0.28	
PICB^N	-69.33	-20.49	-0.79	0.72
CHMZ^N	-69.19	-19.67	1.06	
COLC^N	-68.64	-19.28	0.47	

Table S3: Differences between GPS and InSAR velocities in the final stack. Column 1 shows site name (^{S} indicates GPS stations used to correct the orbital ramp in the southern region and ^{N} indicates GPS station used to correct the orbital ramp in the northern region). Columns 2 and 3 show location of GPS sites (in °). Column 4 contains the differences between the GPS observations (in the LOS direction) ant the InSAR data at same locations in the final stack (in mm/yr). Column 5 contains the RMS of the differences in column 4 for the northern and southern regions (in mm/yr).

compatible with cGPS data and shows a range change pattern that is characteristic of the one expected above a subduction zone, coupled during the interseismic period (Fig. S11). This is another indication of the validity of our atmospheric correction method. The maximum displacement in the satellite line of sight direction can be regarded as a proxy of the projection at the surface of the lower limit of the coupled zone (Fig.S12). Series of cross sections in the InSAR strain rate field show that the distance increases from south to north between the trench and this maximum in LOS displacement, indicating a northward widening of the locked zone (Fig.S11).

3 Modelling

We performed both forward and inverse interseismic models. In order to simulate the kinematic behaviour of the fault plane during the interseismic period, we applied the back-slip assumption (Savage, 1983; Kanda and Simons, 2010), which considers regions locked during the interseismic period as dislocations with opposite sense to that of the coseismic slip. This model assumes that the overriding plate experiences little permanent inelastic deformation on the timescales characteristic of the seismic cycle. We estimate the surface deformation using Okada's formulation (Okada, 1985).

The rigid rotation of the Nazca plate relative to the South American craton is fixed using the pole defined by Vigny et al. (2009) (55.9°N, 95.2°W, 0.610°/My), that predicts a convergence rate of ∼67 mm/yr in the North Chile region. The slip vector on the subduction plane is assumed to be parallel to the convergence (N76°E, Vigny et al., 2009; Sella et al., 2002; Angermann et al., 1999; Norabuena et al., 1999). The interseismic coupling or locking is represented here by the relation between the slip deficit on the megathrust and the long-term slip rate. This parameter describes the kinematic state of the different regions on the megathrust and ranges between 1, in fully locked areas to 0, in areas creeping

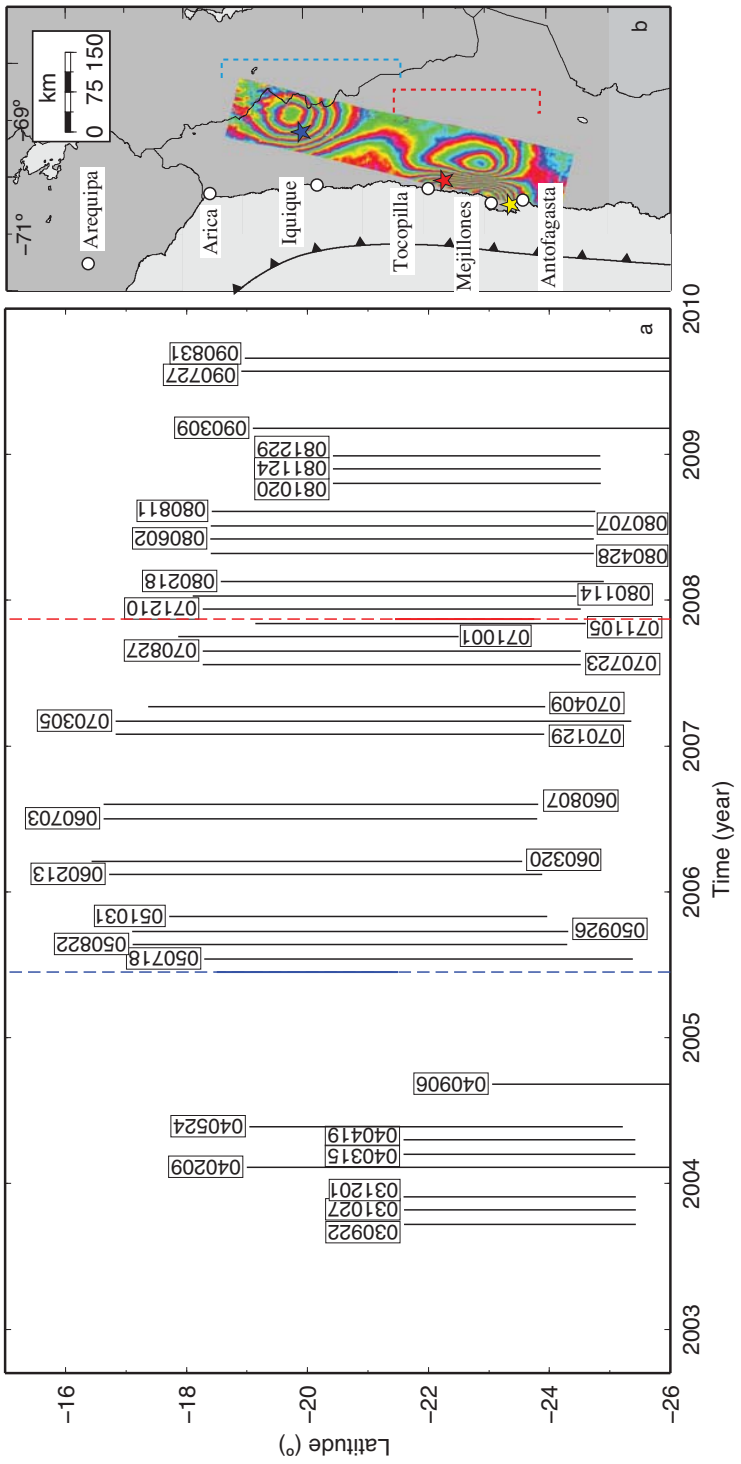

Figure S4: Spatial cover of track 96 ENVISAT images used in this study. (a) Vertical black lines represent acquisition dates and latitudinal extent of individual SAR images. Vertical blue and red dashed lines indicate the date of the 13/06/2005 Tarapacá and 14/11/2007 Tocopilla earthquakes, respectively, with solid segments indicating the latitudinal extent of deformation produced by each earthquake. (b) Surface deformation produced by the 2005 Tarapacá and 2007 Tocopilla earthquakes. Coseismic deformation of the 2005 earthquake dominates north of $\sim$ -21.5° latitude (Peyrat et al., 2006) and coseismic deformation of the 2007 earthquake dominates south of $\sim$ -21.5° latitude (Bejar-Pizarro et al., 2010) (regions delimited by blue and red dashed segments, respectively). The deformation map is formed by two different interferograms that overlaps at -21.5° latitude, with acquisition dates: 24/05/2005 26/09/2005 in the northern region and 5/11/2007-10/12/2007 in the southern region.

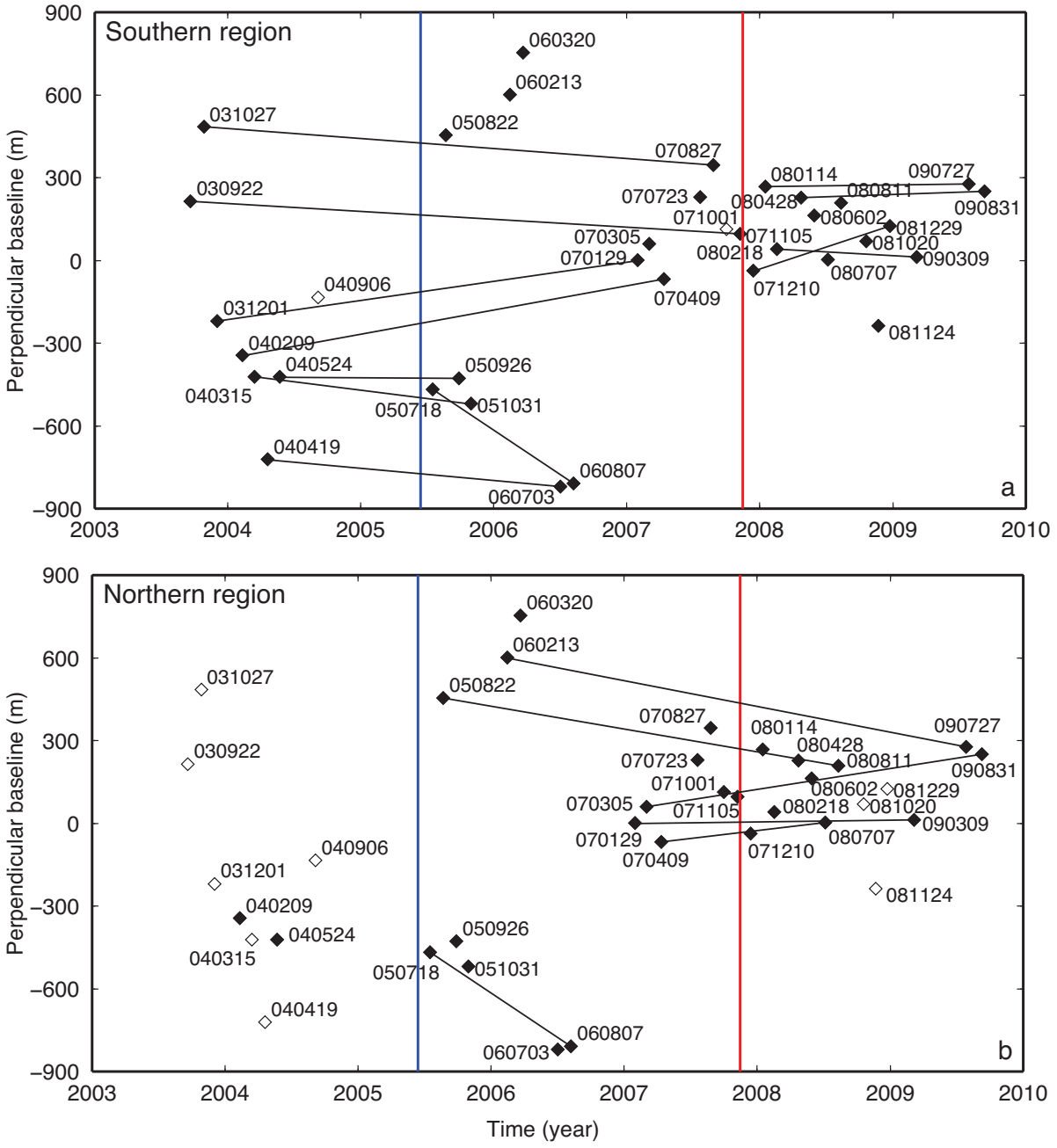

Figure S5: Image acquisition dates as a function of perpendicular baseline for the southern (a) and northern (b) region. The 34 SAR images (diamonds with acquisition dates indicated) are combined into 12 interferograms to study the southern region and 6 interferograms to study the northern region (black segments in a and b, respectively). Only combinations with perpendicular baselines smaller than 350 m and temporal baselines larger than 1 year are considered. The temporal span of interferograms is limited to avoid contamination of the interseismic signal from coseismic deformation related to the 2005 Tarapacá earthquake in the northern region (vertical blue line) and the 2007 Tocopilla earthquake in the southern region (vertical red line). White diamonds represent SAR images not used to build interferograms because they not fit the criteria.

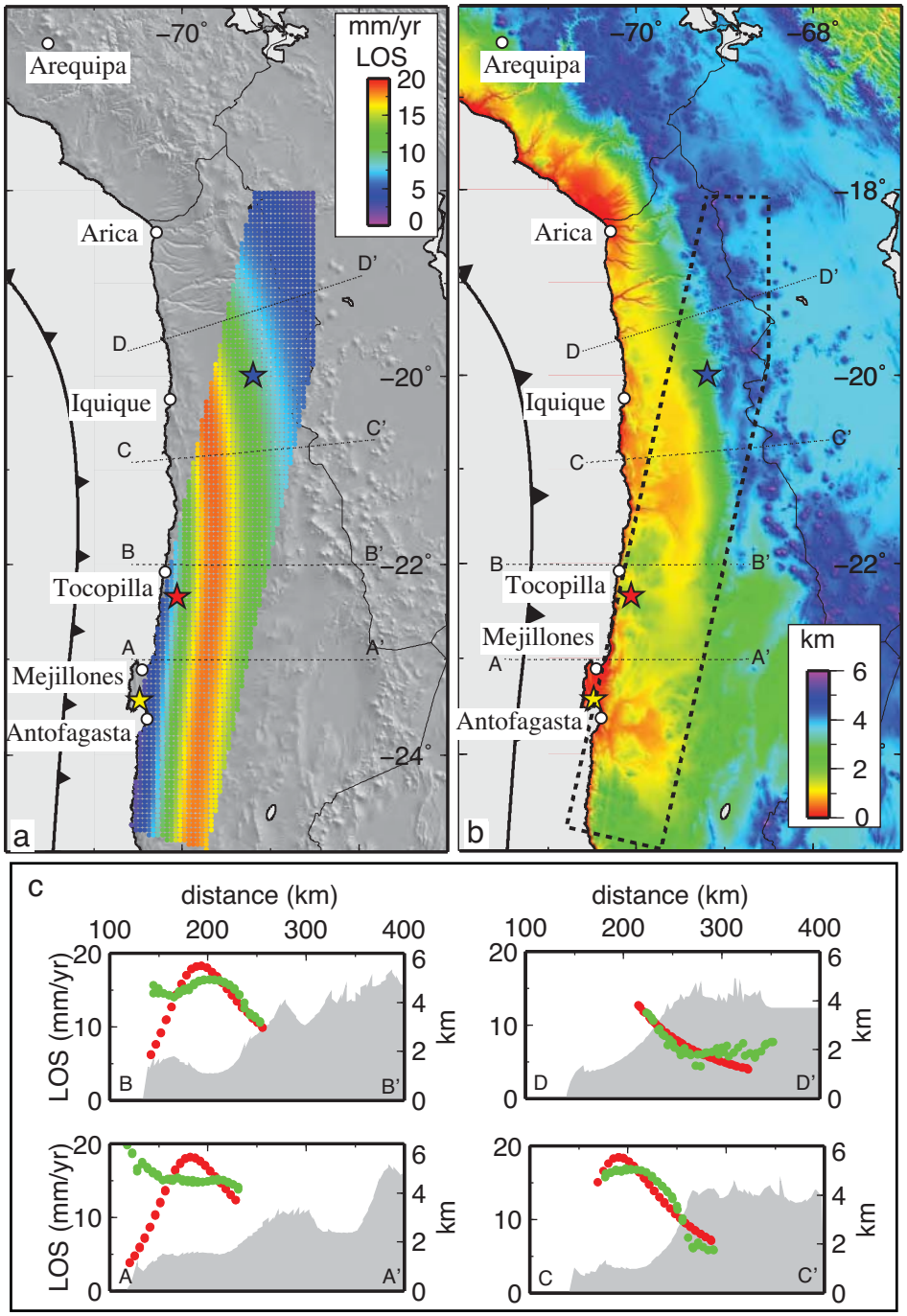

Figure S6: Comparison of interseismic deformation predicted by a simple elastic model (a) and topography in the region (b). We estimate the surface deformation in the satellite line of sight direction predicted by a simple coupling model, with megathrust fully locked between trench and 50 km depth (corresponding to coupling distribution model A, Fig. S13). (c) Cross sections indicated in (a) and (b), showing the predicted interseismic deformation (red points), the topography (grey region) and the inverted topography in the same points where interseismic deformation is estimated (green points). A clear correlation between the predicted deformation and the inverted topography is revelled. The eastern slope of the deformation field approximately coincides with the mayor topographic slope, a region where the atmospheric signals related with topography tend to be important.

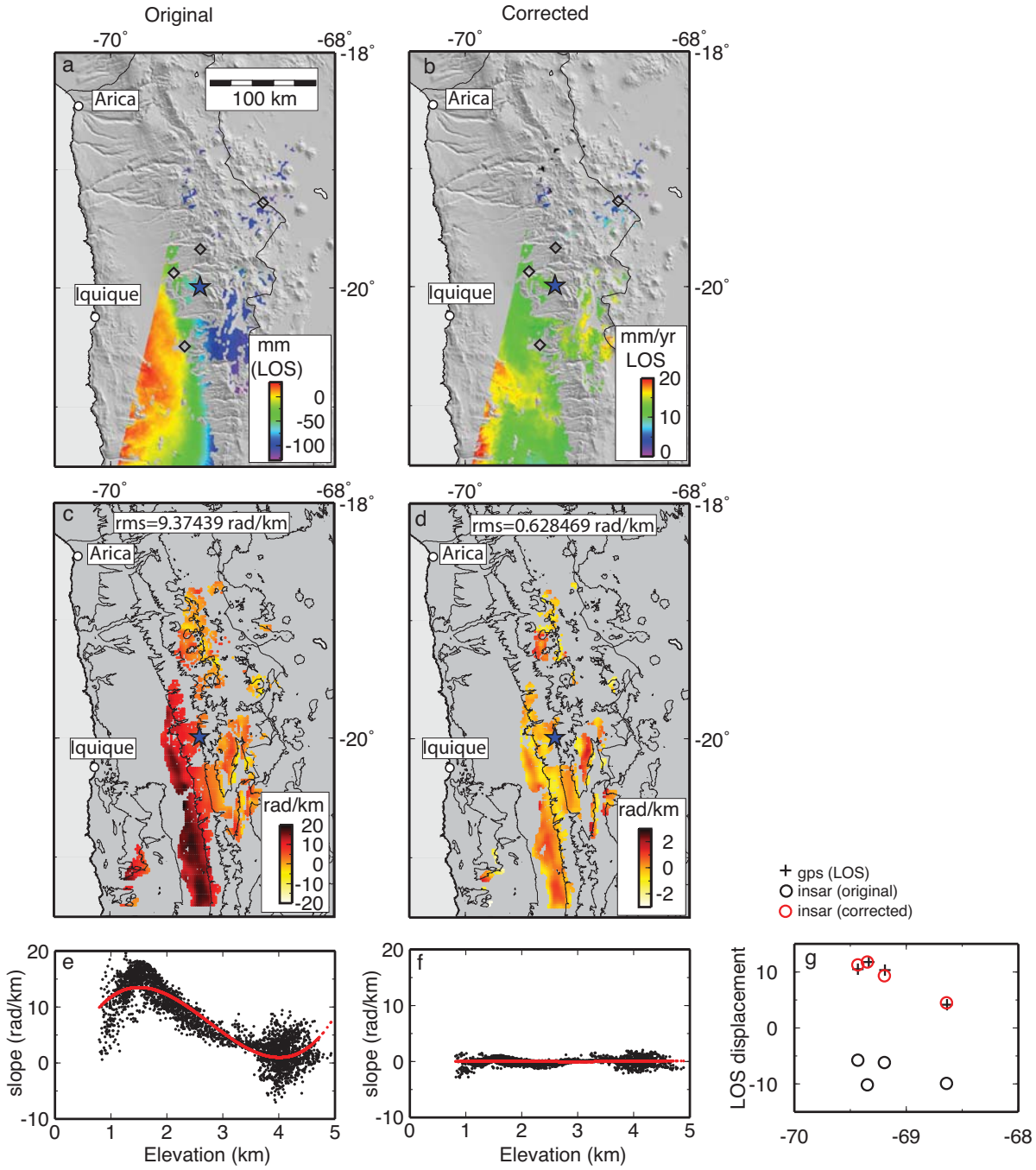

Figure S7: Example of corrections applied to one of the interferograms used in the stack. The example corresponds to an interferogram with acquisition dates 13/02/2006 and 27/07/2009. (a) Original interferogram. (b) Interferogram after two consecutive atmospheric and orbital corrections. (c) and (d) Slopes (phase/elevation) estimated in little windows in the interferograms. Slopes are not estimated in region with altitude difference smaller than 100 m. Rms values are also indicated. (e) (f) Black points represent the slopes (phase/elevation) estimated in each window in function of elevation, for the original (e) and the corrected interferogram (f). Red line represents the tropospheric delay estimated using a polynomial. (g) Effect of removing a linear phase ramp in the interferogram, to simulate the effect of the orbital baseline adjustment, using the GPS velocities contained in the interferogram as a reference (four black diamonds in (a) and (b)). We project the GPS velocities into the satellite line of sight direction (black crosses) and compare them with the InSAR velocities in the same four locations, represented by the black and red circles (before and after removing the phase ramp, respectively).

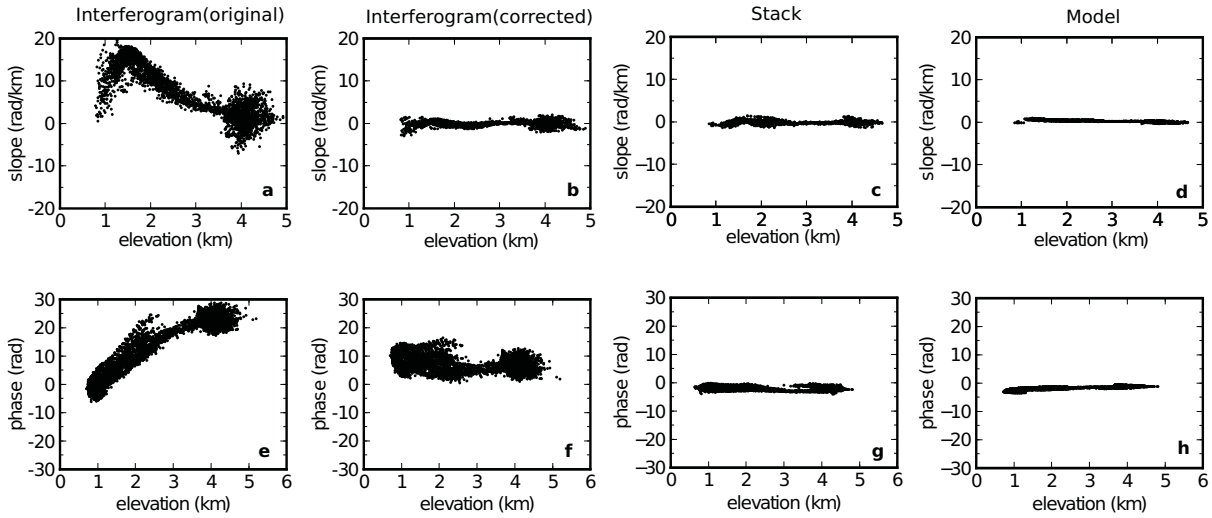

Figure S8: a-d, Variation of slopes (phase/elevation) with elevation estimated in small windows (10x10 km) for one interferogram (same as in Fig. S7) before (a) and after (b) correction, the stack (c) and a model (d, model D in Fig. S14).e-h , Phase/elevation relationship for the same interferogram, stack and model.

with the interplate rate during the interseismic period.

Shortening in the Central Andes is mainly localized in the Subandean thrust-belt regions, according to geological and geodetic studies (Brooks et al., 2011; Chlieh et al., 2011; Baby et al., 1997; Kley and Monaldi, 1998; Bevis et al., 2001; Chlieh et al., 2004; Khazaradze and Klotz, 2003; Klotz et al., 1999; Norabuena et al., 1998). The magnitude of this shortening significantly varies (3 - 15 mm/yr) depending on the study and we cannot resolve it with our data set (∼600 km away from the subandean region). We have tested both, a configuration without taking into account this shortening (using a 2-plate model) and a configuration with 3 plates, including a sliver rigid block between the Nazca and the South American plates and a shortening velocity of 1 cm/yr (Brooks et al., 2011; Chlieh et al., 2011). Comparing the results, the 3-plate configuration reduces the GPS horizontal residuals in the eastern part of our region and requires less coupling to fit our interseismic velocities, although the coupling distribution pattern does not change between the 2-plate and the 3-plate model. In the next section, all forward models are constructed using a 2-plate configuration, except for one case (model E) constructed with a 3-plate configuration and a variable shortening rate to test the robustness of the results (see Fig. S16 and next section for details). All the inversions are constructed with a 3-plate configuration and a shortening velocity in the subandean ranges of 1 cm/yr (a constant translation value applied to both the measured velocities and the convergence rate used in the models).

We use two different geometries for the fault plane:

- a uniformly dipping fault plane with the updip edge being consistent with the trench location.

- we also test the geometry proposed by Contreras-Reyes et al. (2012), characterized by an abrupt change (from 10° to 22°) in the dip of the fault plane.

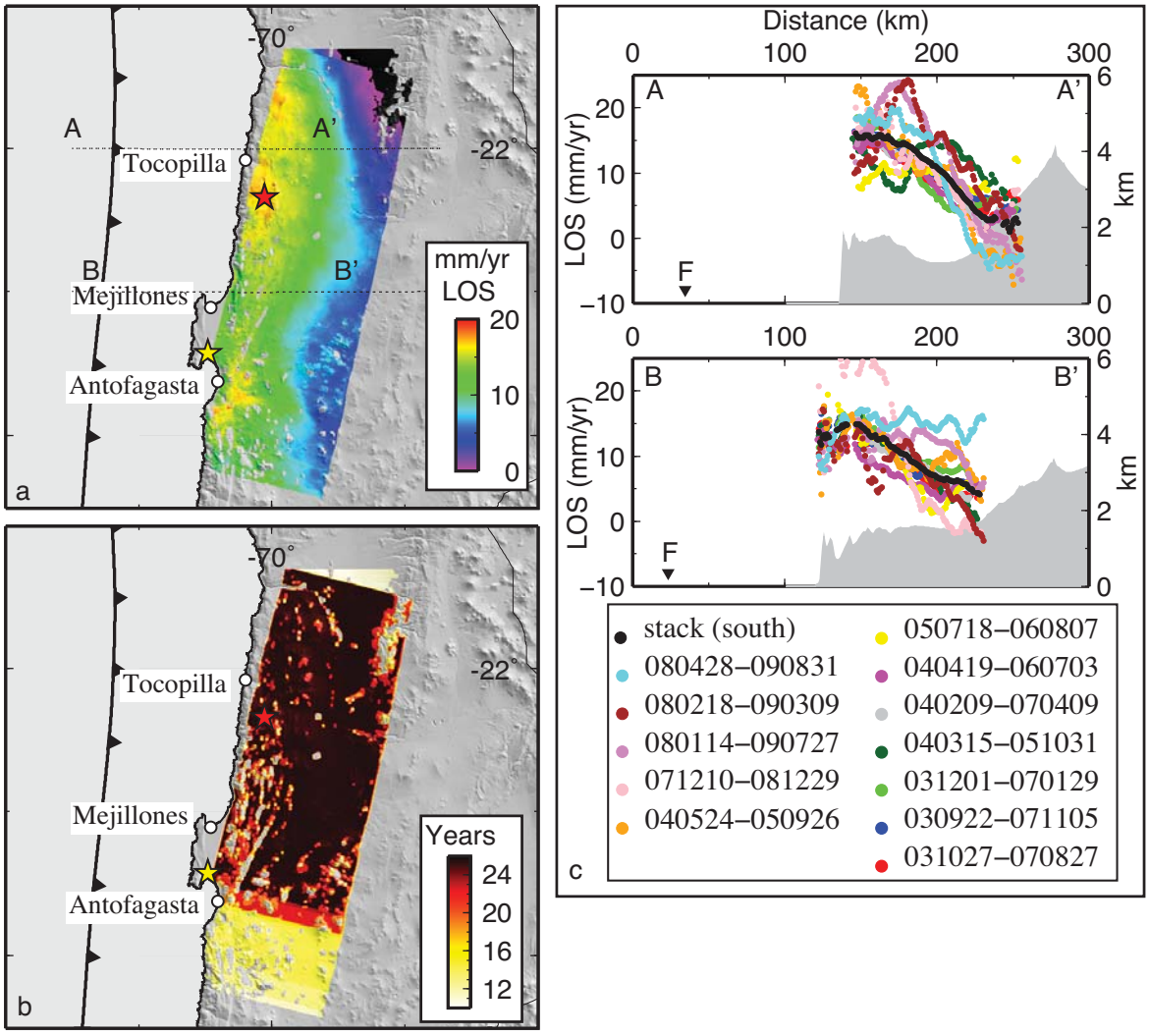

Figure S9: (a) Stack for the southern region. The average velocity has been calculated by summing interferograms (in mm/yr) that are coherent for a given pixel divided by the number of interferograms summed (b) Cumulative duration of interferograms which are coherent at each pixel. Only pixels with a cumulative time larger than 10 years are selected for the final stack. Most of the pixels in the stack have more than 20 years of cumulated time. (c) Cross sections indicated in (a) comparing the stack with the individual interferograms summed.

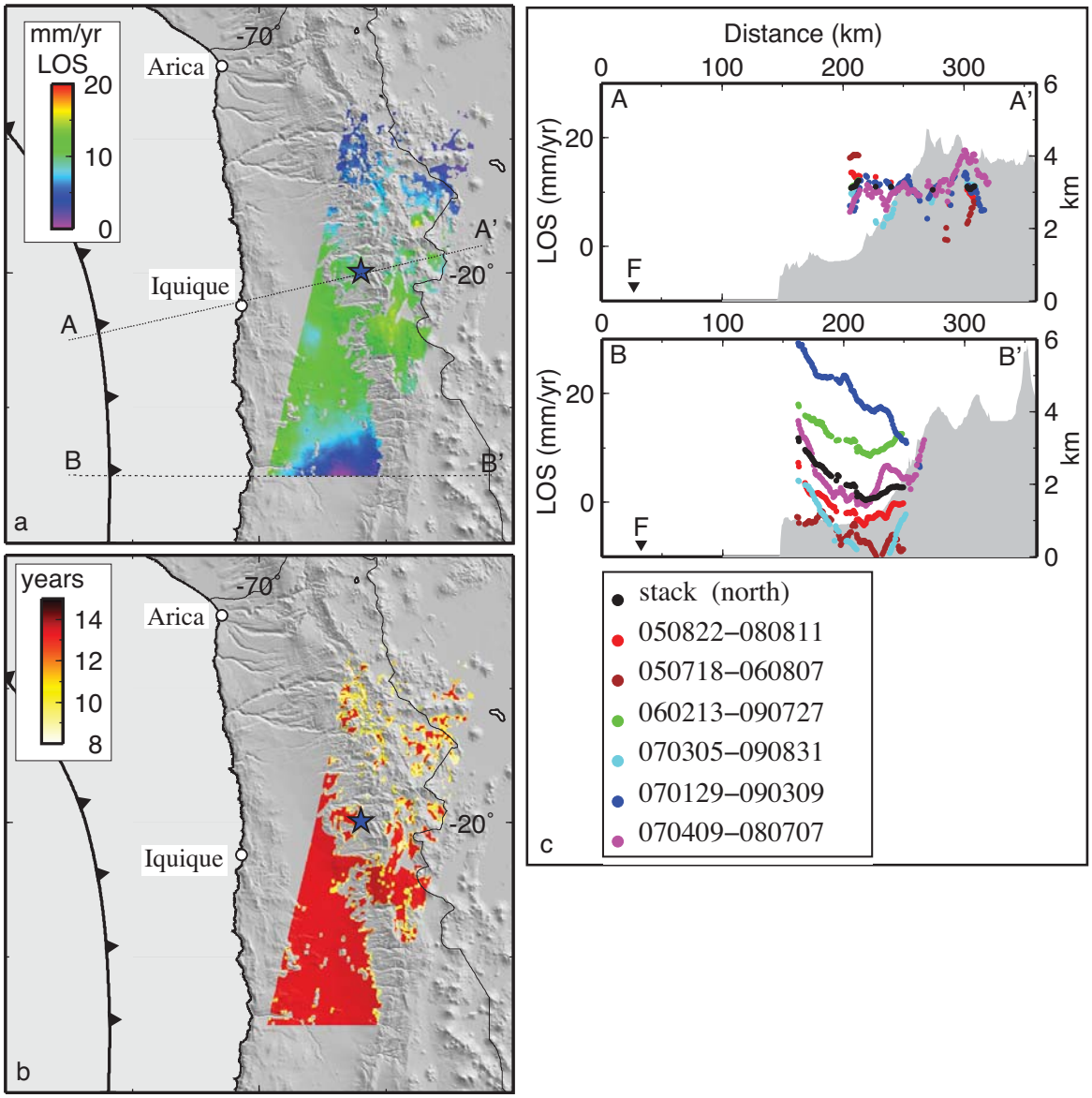

Figure S10: (a) Stack for the northern region. (b) Cumulative duration of interferograms which are coherent at each pixel. Only pixels with a cumulative time larger than 8 years are selected for the final stack. Most of the pixels in the stack have more than 13 years of cumulated time. (c) Cross sections indicated in (a) comparing the stack with the individual interferograms summed.

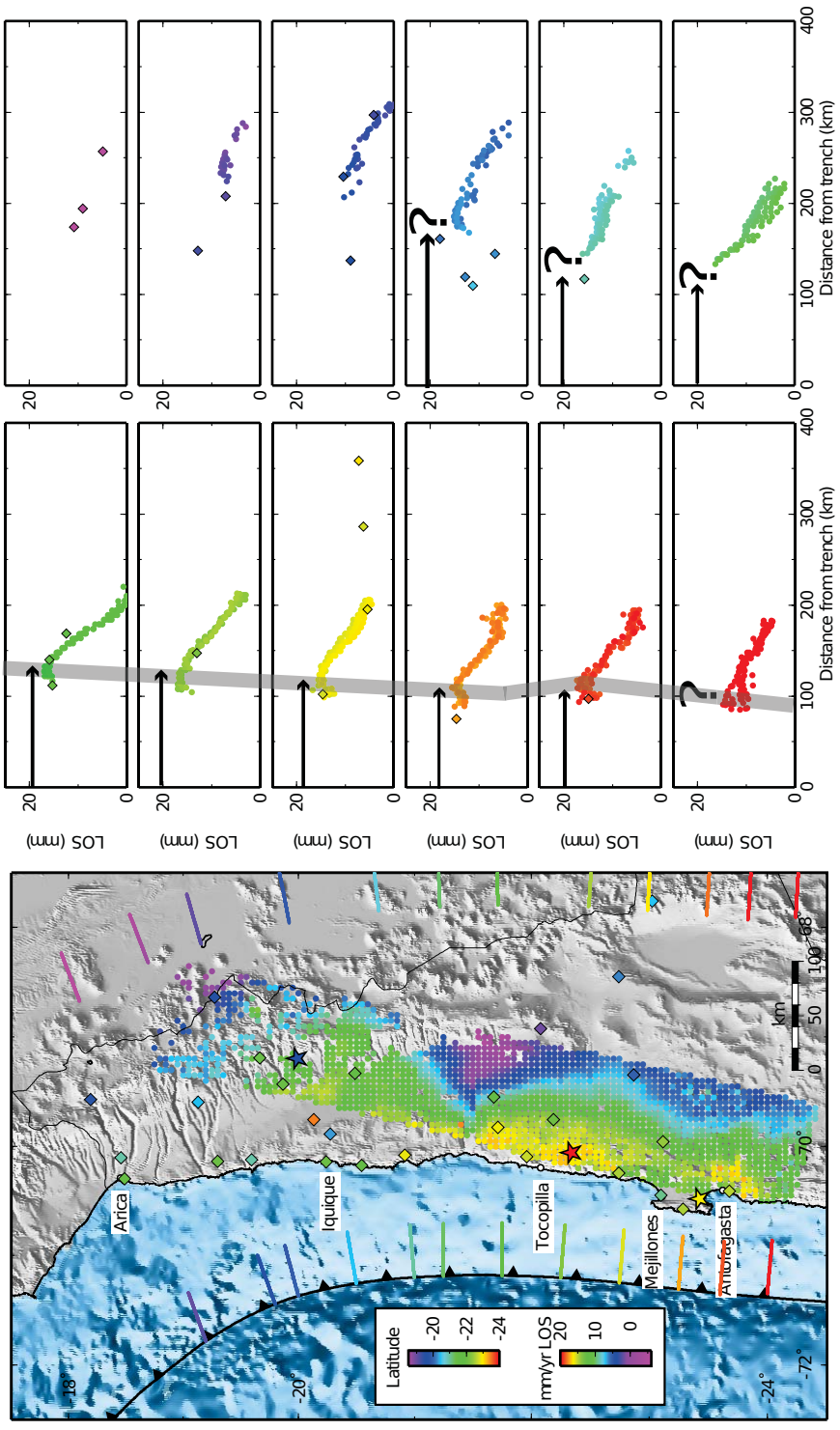

Figure S11: (Left) Interseismic deformation field measured by InSAR, obtained from the two partial stacks for the southern and northern region (Figs. S9 and S10). GPS velocities have been projected in the satellite's line of sight (coloured diamonds). (Right) LOS velocities along the 12 cross-sections indicated in the map. Horizontal black arrows indicate distance between the trench and the maximum in LOS displacement. The location of this maximum is unequivocal south of -21° latitude, but less clear north of this latitude (black question marks), probably due to the scarcity of data in this region. The distance between the trench and the maximum in LOS displacement (indicated by the gray transparent segment) increases from south to north, indicating a northward widening of the locked zone.

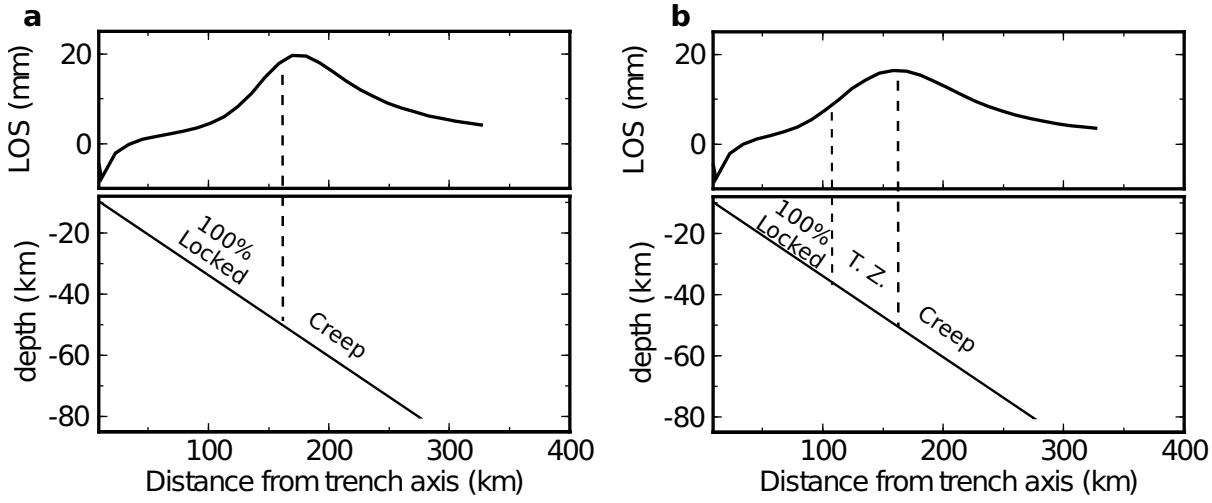

Figure S12: 2D-profiles showing the LOS displacement predicted by two simple forward back-slip models of interseismic deformation. (a) and (b) show the LOS deformation above the dislocation, without (a) and with (b) a transition zone between the shallow fully locked region and the deeper creeping region on the megathrust. (a) corresponds to cross section 4 in model A and (b) correspond to cross section 4 in model B (see Fig. S13).

3.1 Forward Models

We have built several simple forward back-slip models of interseismic deformation to compare the surface deformation in the satellite LOS direction predicted by these models with our velocity field.

Our two first forward models (A and B, Fig. S13) aim at testing the coupling models previously published for the area. The base of the coupled region is parallel to the trench, with (model B) or without (model A) a transition zone between the shallow fully locked region and the deeper creeping region on the megathrust (e.g., Chlieh et al., 2004; Bevis et al., 2001). The base of the locked zone in model A is located at 50 km depth and the transition zone in model B is located between 35 - 55 km depth.

The other two models (C and D, Fig. S14) test an alternative hypothesis, where the base of the coupled region is parallel to the coastline. We test this hypothesis with either a uniformly dipping fault plane (model C), or with an abrupt change in the dip of the subduction plane, as proposed by Contreras-Reyes et al. (2012) (model D).

The synthetic deformation predicted by these models is compared to the data along cross section in Fig. S15. Models C and D explain the observed deformation field and its lateral changes while models A and B fail to reproduce it.

Additionally we have tested the influence of variable shortening rate along the subandean thrusts in the locking depth (model E, Fig. S16). For that, we use the coupling distribution in model B and a 3-plate configuration with an Euler pole inducing a shortening of 3 to 15 mm/yr from south to north in our region. The new model predicts an interseismic deformation very similar in shape to deformation in model B (Fig. S16) but it presents a magnitude that decreases from south to north (due to the shortening rate increase in this direction). Note that deformation predicted by model E in Fig. S16 has been referenced to South-America frame in order to compare this deformation with the estimated velocity field and with deformation predicted by model B (2-plate configuration).The location of the

maximum in LOS displacement does not change in the new model, failing to explain the estimated velocity field. This suggests that the variable shortening has no influence in the location of the locking depth that seems to be mainly controlled by the position of the maximum InSAR LOS rate. On the contrary, the amount of shortening in the subandean ranges influences the amount of coupling.

3.2 Inversion procedure

To invert our interseismic geodetic measurements for the coupling distribution pattern on the megathrust, we use the geometry of the subduction interface defined by Contreras-Reyes et al. (2012) (model D in Fig. S13). We divide the megathrust interface into an array of 31 x 19 elements, each measuring $\sim$ 25 x 30 km (although patches length vary locally to mimic the curvature of the subduction interface at the latitude of the Arica bend). To solve for the locking coefficient along the 589 patches we use a least-squares minimization with the non-negativity constraint on the slip. We impose a constant direction of slip (parallel to the convergence direction: N76°) in all patches and the locking coefficient is allowed to vary from 0 to 1 in each patch. To limit oscillations of the solution, we impose some smoothing on the solution, by minimizing the second-order derivative of the fault slip (e.g., Harris and Segall, 1987; Du et al., 1992; Arnadottir and Segall, 1994; Grandin et al., 2009). We also forced the locking coefficient to vanish at the bottom of the fault plane. We perform independent inversions for each data set as well as joint inversions. For the joint inversion of the InSAR and cGPS data we experiment with different weighting. We search for a compromise between the rms (that should be similar in both data sets) and the spatial density of each type of data. We determine the optimal solution roughness that will be used in our final models searching for a compromise between the roughness and the misfit of the solution (e.g., Menke, 1989; Jonsson et al., 2002). The optimal roughness value determined from the trade-off curve is shown in Fig. S17a. Inversion results for each data set are shown in Fig. S18. The rate of moment deficit of our best model over the 1877 segment (Fig. S18c) is 8.15 x 10e +19 Nm/yr (assuming an averaged shear modulus of 33 GPa). If we assume this moment deficit rate is approximately steady since the 1877 rupture, it leads to a moment of 1.1 x 10e +22 Nm, equivalent to a Mw $\sim$8.6 event.

We also tested inversions on a uniformly dipping fault plane (dip angle =15°, similar to models A, B and C in Figs S13 and S14). The coupling pattern obtained from joint inversion of the GPS and InSAR data (Fig. S19) is very consistent with the coupling pattern obtained using the non-uniformly dipping plane (Fig. S18). In both models, the lower limit of the coupling is parallel to the coastline and the seismogenic zone seems to be wider although less coupled towards the north.

3.3 Spatial resolution of the formal inversion

We examined the spatial resolution of our models through various checkerboard tests. To evaluate the capacity of each data set to solve for the coupling coefficient on the fault plane, we divided the megathrust interface in rectangular patches and assigned each patch a coupling coefficient of either 1 (fully locked patches) or 0 (patches creeping at the plate convergence rate) (Figs S20a and S21a).

The surface deformation due to each one of these models is then computed at all the locations where we have GPS and InSAR observations. These simulated data sets are inverted for coupling coefficient using the procedure described above. Figs S20 and S21 show the results of the inversions using each type of data separately and jointly, for the fault plane with an abrupt change in dip and the fault plane with a uniform dip, respectively.

In general, we can recover the input pattern of slip on portions of the subduction zone that lie beneath our geodetic measurements. The lower spatial resolution of GPS inversion compared to InSAR inversions

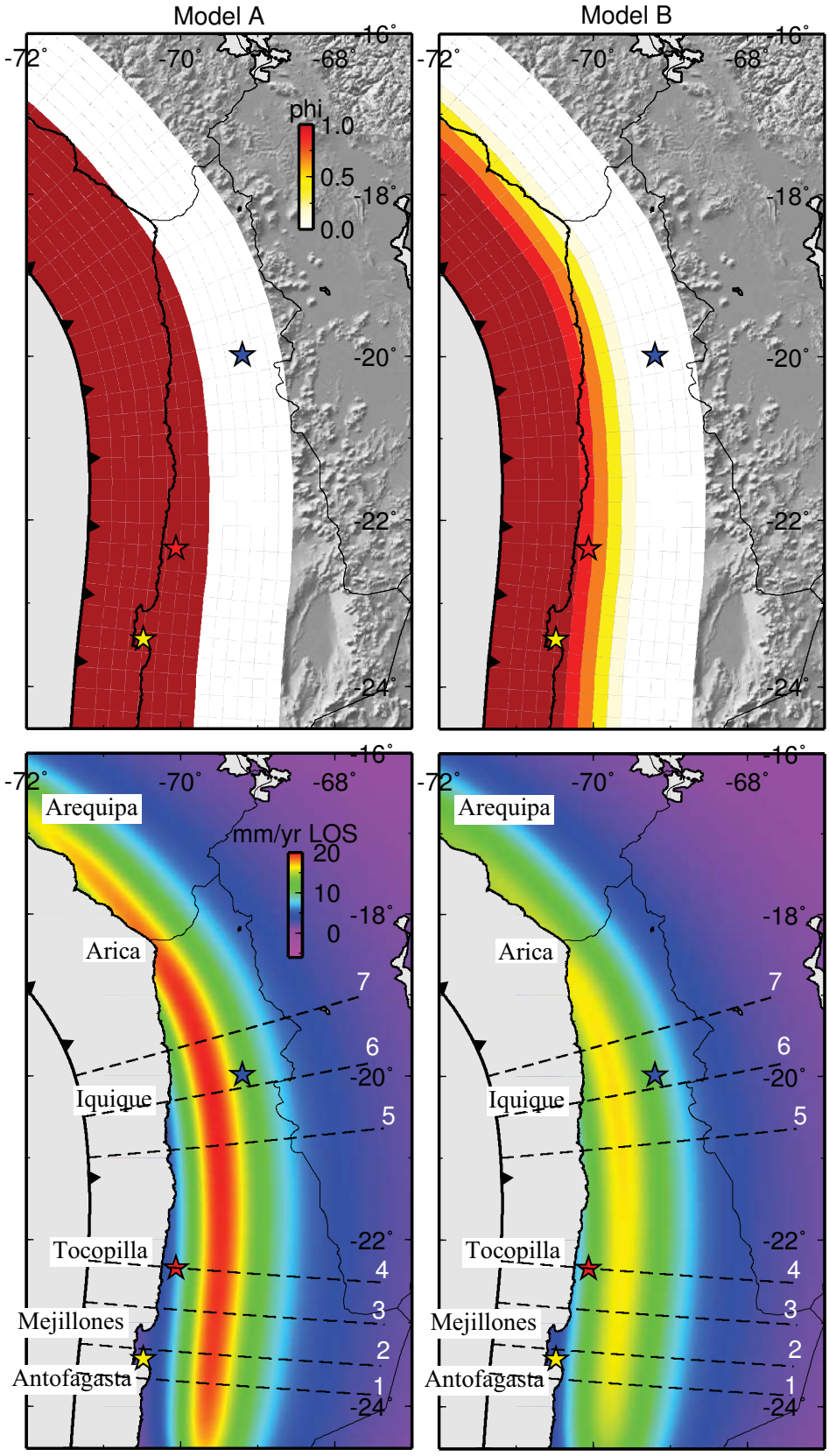

Figure S13: Forward models with base of the coupled region parallel to the trench. Model A has no transition zone while model B has a transition zone between 35 - 55 km depth. The 2 upper maps represent the coupling coefficient on the subduction interface, and the 2 lower maps represent the deformation predicted by the models projected in the satellite line of sight (to be compared with InSAR data).

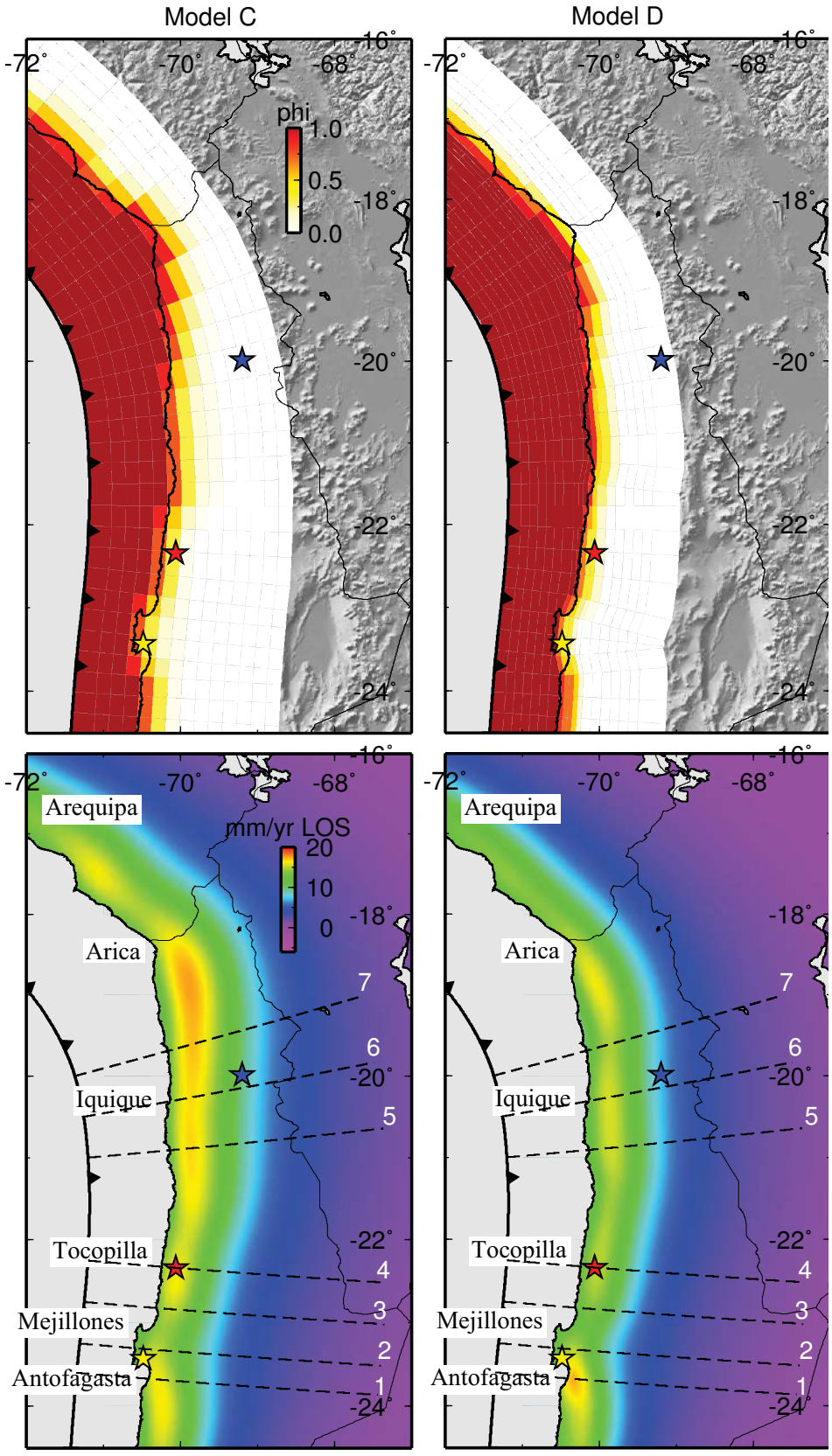

Figure S14: Forward models with base of the coupled region parallel to the coast. Model C has a uniform dip of 15° and model D has an abrupt change (from 10° to 22°) in the dip of the fault plane (suggested by Contreras-Reyes et al., 2012). The 2 upper maps represent the coupling coefficient on the subduction interface, and the 2 lower maps represent the deformation predicted by the models projected in the satellite line of sight (to be compared with InSAR data)

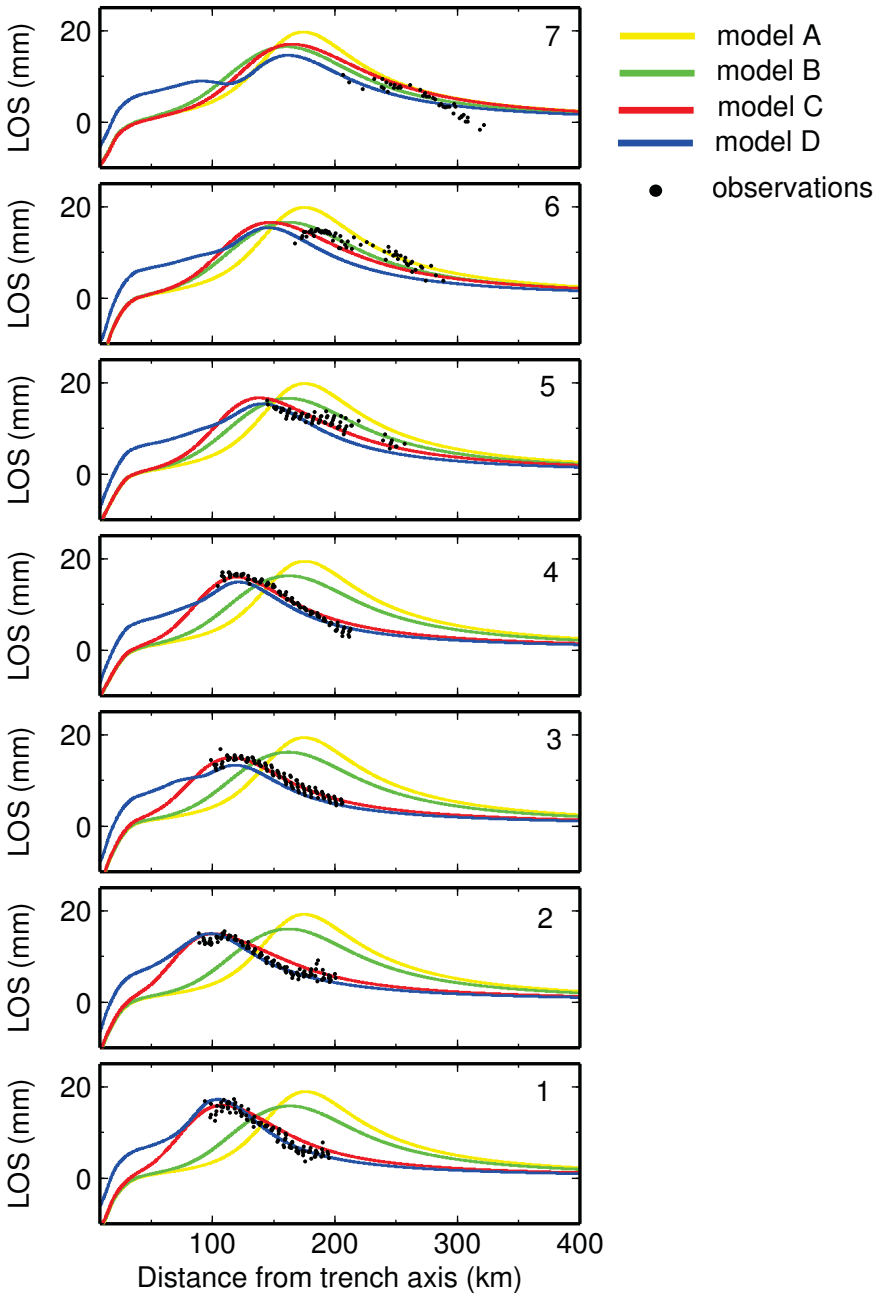

Figure S15: Cross sections perpendicular to the trench showing deformation predicted by A, B, C and D forward models of interseismic deformation (colour lines) compared with the estimated InSAR velocity field (black points).

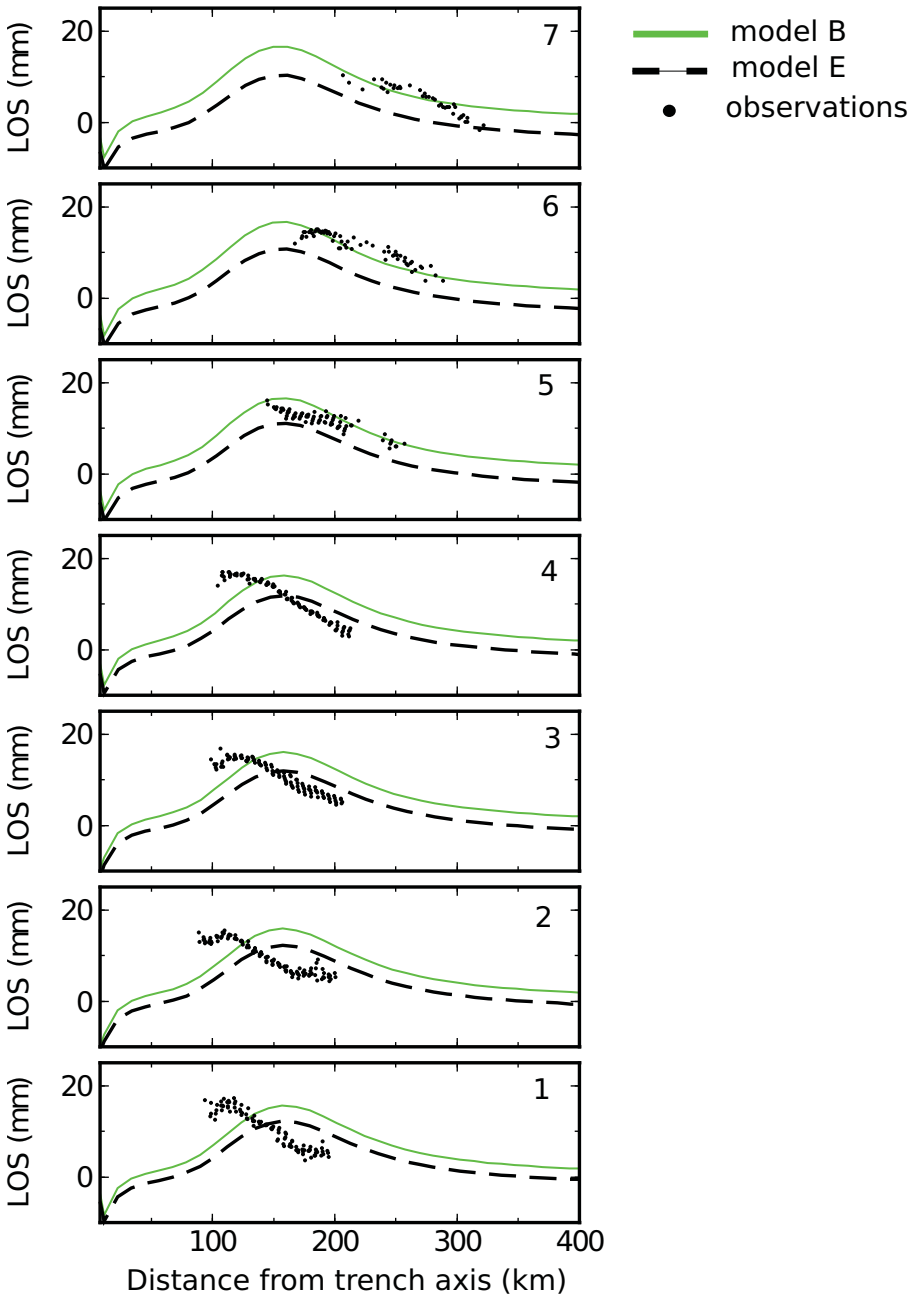

Figure S16: Cross sections perpendicular to the trench comparing deformation predicted by forward models B (green lines) and E (dashed black lines) with the estimated InSAR velocity field (black points). Both models assume a transition zone between 35 - 55 km depth. Model B does not consider shortening across the subandean ranges while model E assumes a shortening varying from 3 mm/yr (at latitude -24°) to 15 mm/yr (at latitude -16°). This test shows that the location of the maximum LOS deformation is not affected by the amount of convergence across the subandean ranges. On the other hand, the value of the peak deformation is smaller in model E, and decreases from south (where intracontinental shortening is 3 mm/yr) to north (where intracontinental shortening is 15 mm/yr).

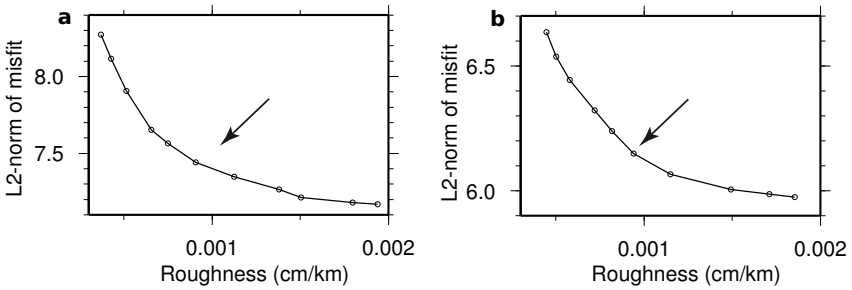

Figure S17: Tradeoff curves between the residual L2 norm and the model roughness for the inversions using a plane with an abrupt change in dip (a) and a uniformly dipping fault plane (b). The arrows mark the chosen roughness value in each case.

is obvious, as expected due the different data coverage. We have no resolution for the northernmost and the southernmost part of the slab, due to the lack of data covering these regions. The shallowest (from the trench to 10-15 km depth) and the deepest (beneath 60-65 km depth) parts of the interface are poorly resolved. All these poorly resolved areas have been masked out in the inversions results (semi-transparent gray areas in Figs S18 and S19).

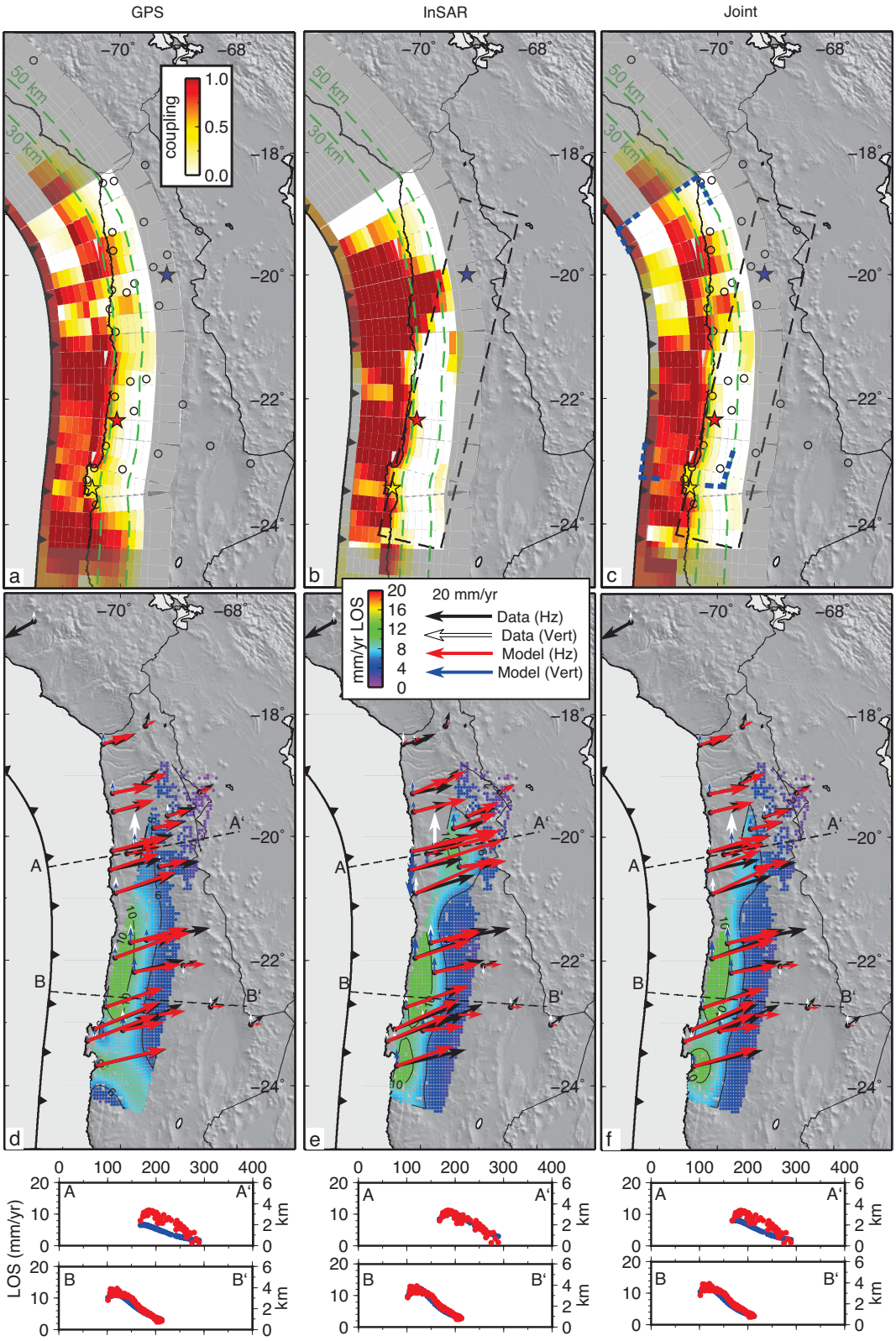

Figure S18: (a -c) Distribution of coupling on the North Chile subduction zone derived from the formal inversion of GPS and InSAR velocities. Fully locked areas are red, and fully creeping areas are white. Black circles in (a) and (c) represent the GPS stations used in the inversion. Dashed black rectangle in (b) and (c) delimit the approximate area covered by the InSAR data. Dashed green lines are the slab isodepth. Semi-transparent gray areas mask poorly resolved parts of the slab (see section 3.3). Dashed blue segments in (c) limit the region used to estimate the rate of moment deficit.(d-f) Vectors represent observed and predicted GPS velocities. Cross-sections perpendicular to the trench (A-A' and B-B') show observed (red dots) and modelled (blue dots) LOS velocities.

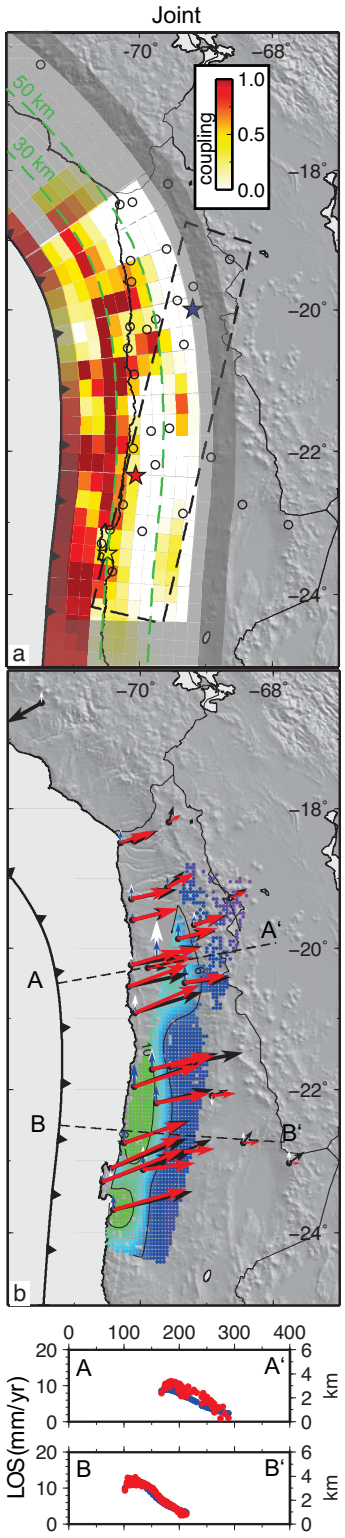

Figure S19: (a) Distribution of coupling on the North Chile subduction zone derived from joint inversion of GPS and InSAR velocities, using a fault plane with a uniform dip angle of 15°. (b) Vectors represent observed and predicted GPS velocities. Cross-sections perpendicular to the trench (A-A' and B-B') show observed (red dots) and modelled (blue dots) LOS velocities. See text in Fig. S18 for more details.

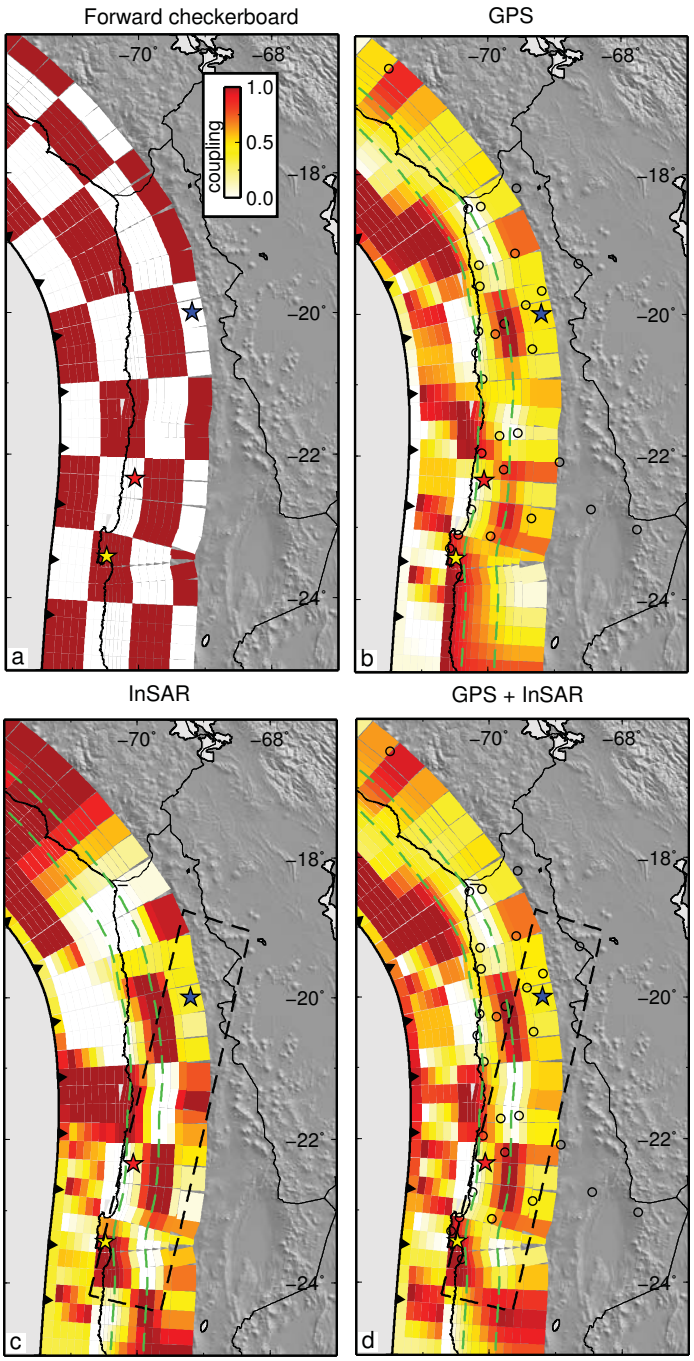

Figure S20: Checkerboard resolution test for the fault plane with an abrupt change in dip. (a) Synthetic slip model used in the resolution test. Size of rectangular patches is ∼ 110x65 km. We compute the predicted displacements of this model at the locations of our GPS and InSAR observations. The synthetic SAR data are subsampled in the same fashion as the observed data. (b), (c) and (d) Coupling distributions obtained from inversions using (b) only GPS data, (c) only InSAR data and (d) InSAR and GPS data jointly. Black circles in (b) and (d) represent the GPS stations used in the inversion. Dashed black rectangle in (c) and (d) delimit the area covered by the InSAR data.

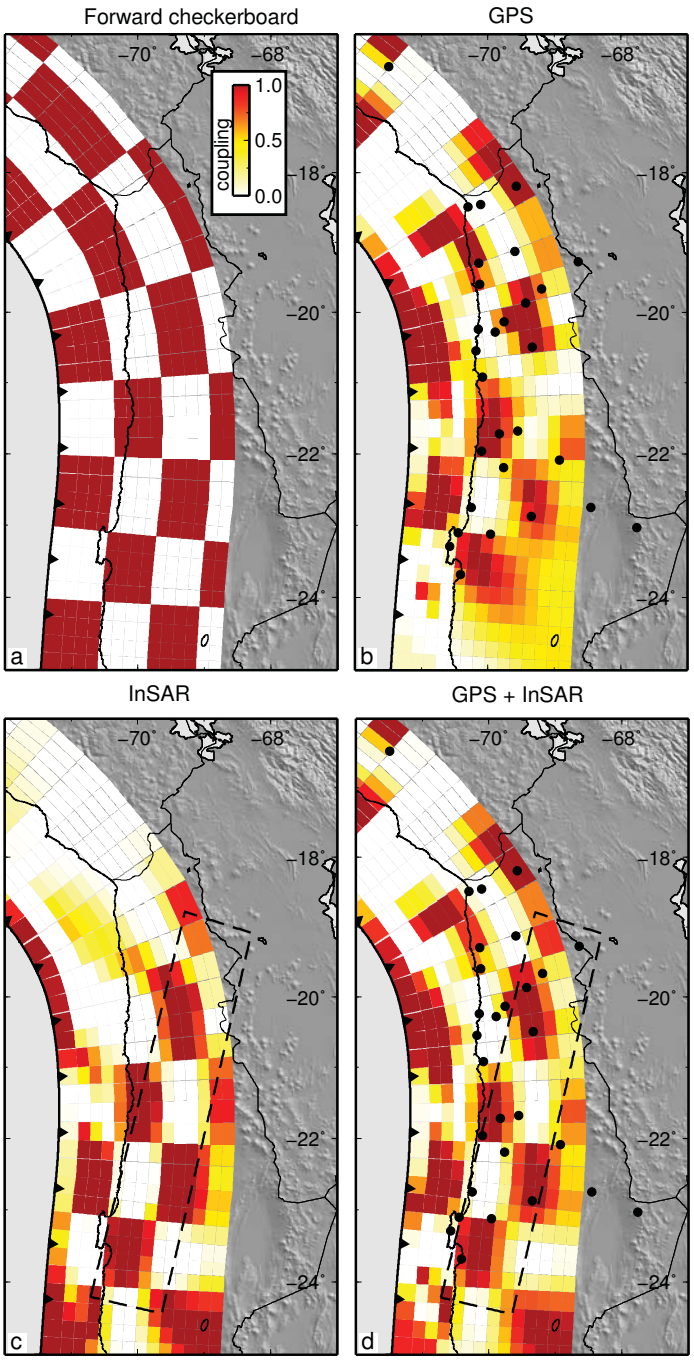

Figure S21: Checkerboard resolution test for the uniformly dipping fault plane. (a) Synthetic slip model used in the resolution test. Size of rectangular patches is ∼ 110x120 km. We compute the predicted displacements of this model at the locations of our GPS and InSAR observations. The synthetic SAR data are subsampled in the same fashion as the observed data. (b), (c) and (d) Coupling distributions obtained from inversions using (b) only GPS data, (c) only InSAR data and (d) InSAR and GPS data jointly. Black circles in (b) and (d) represent the GPS stations used in the inversion. Dashed black rectangle in (c) and (d) delimit the area covered by the InSAR data.

References

Altamimi, Z., Collilieux, X., Legrand, J., Garayt, B., and Boucher, C. (2007). ITRF2005: A new release of the International Terrestrial Reference Frame based on time series of station positions and Earth Orientation Parameters. *J. Geophys. Res.*, 112:B09401.

Angermann, D., Klotz, J., and Reigber, C. (1999). Space-geodetic estimation of the Nazca-South America Euler vector. *Earth Planet. Sci. Lett.*, 171:329–334.

Arnadottir, T. and Segall, P. (1994). The 1989 Loma Prieta earthquake imaged from inversion of geodetic data. *J. Geophys. Res.*, 99(B11):21835–21855.

Baby, P., Rochat, P., Mascle, G., and Herail, G. (1997). Neogene shortening contribution to crustal thickening in the back arc of the Central Andes. *Geology*, 25:883–886.

Bejar-Pizarro, M., Carrizo, D., Socquet, A., Armijo, R., Barrientos, S., Bondoux, F., Bonvalot, S., Campos, J., Comte, D., De Chabalier, J. B., Charade, O., Delorme, A., Gabalda, G., Galetzka, J., Genrich, J., Nercessian, A., Olcay, M., Ortega, F., Ortega, I., Remy, D., Ruegg, J. C., Simons, M., Valderas, C., and Vigny, C. (2010). Asperities and barriers on the seismogenic zone in North Chile: state-of-the-art after the 2007 Mw 7.7 Tocopilla earthquake inferred by GPS and InSAR data. *Geophys. J. Int.*, 183:695–711.

Bevis, M., Kendrick, E., Smalley, R., Brooks, B., Allmendinger, R., and Isacks, B. (2001). On the strength of interplate coupling and the rate of back arc convergence in the central Andes: An analysis of the interseismic velocity field. *Geochem. Geophys. Geosyst.*, 2(11):1067.

Brooks, A., Bevis, M., Whipple, K., and Arrowsmith, J. R. (2011). Orogenic-wedge deformation and potential for great earthquakes in the central Andean backarc. *Nature Geosci.*, 4:380–383.

Chlieh, M., de Chabalier, J. B., Ruegg, J. C., Armijo, R., Dmowska, R., Campos, J., and Feigl, K. L. (2004). Crustal deformation and fault slip during the seismic cycle in the North Chile subduction zone, from GPS and InSAR observations. *Geophys. J. Int.*, 158:695–711.

Chlieh, M., Perfettini, H., Tavera, H., Avouac, J. P., Remy, D., Nocquet, J. M., Rolandone, F., Bondoux, F., Gabalda, G., and Bonvalot, S. (2011). Interseismic coupling and seismic potential along the Central Andes subduction zone. *J. Geophys. Res.*, 116:B12405.

Contreras-Reyes, E., Jara, J., Grevemeyer, I., Ruiz, S., and Carrizo, D. (2012). Abrupt change in the dip of the subducting plate beneath north Chile. *Nature Geosci.*, 5:342–345.

Doin, M., Lasserre, C., Peltzer, G., Cavalie, O., and Doubre, C. (2009). Corrections of stratified tropospheric delays in SAR interferometry: Validation with global atmospheric models. *J. Appl. Geophys.*, 69:35–50.

Dong, D., Fang, P., Bock, Y., Cheng, M. K., and Miyazaki, S. (2002). Anatomy of apparent seasonal variations from GPS-derived site position time series. *J. Geophys. Res.*, 107:2075.

Du, Y., Aydin, A., and Segall, P. (1992). Comparison of various inversion techniques as applied to the determination of a geophysical deformation model for the 1983 Borah Peak earthquake. *Bull. Seismol. Soc. Am.*, 82:1840–1866.

Farr, T. G. and Kobrick, M. (2000). Shuttle Radar Topography Mission produces a wealth of data. *EOS, Trans. Am. geophys. Un.*, 81:583–585.

Fournier, T. J., Pritchard, M. E., and Finnegan, N. J. (2011). Accounting for atmospheric delays in InSAR data in a search for long wavelength deformation in South America. *IEEE Trans. Geosci. Remote Sens.*, 49:3856–3867.

Grandin, R., Socquet, A., Binet, R., Klinger, Y., Jacques, E., de Chabalier, J., King, G. C. P., Lasserre, C., Tait, S., Tapponnier, P., Delorme, A., and Pinzuti, P. (2009). September 2005 Manda Hararo-Dabbahu rifting event, Afar (Ethiopia): Constraints provided by geodetic data. *J. Geophys. Res.*, 114:B08404.

Hanssen, R. (2001). *Radar Interferometry, Data Interpretation and Error Analysis*. Kluwer Academic Publishers.

Harris, R. A. and Segall, P. (1987). Detection of a locked zone at depth on the Parkfield, California, segment of the San Andreas fault. *J. Geophys. Res.*, 92:7945–7962.

Herring, T. A. (2002). *GLOBK: Global Kalman filter VLBI and GPS analysis program,version 10.0*. MIT, Cambridge, MA.

Jonsson, S., Zebker, H., Segall, P., and Amelung, F. (2002). Fault slip distribution of the 1999 Mw 7.1 Hector Mine, California, earthquake, estimated from satellite radar and GPS measurements. *Bull. Seismol. Soc. Am.*, 92:1377–1389.

Kanda, R. V. S. and Simons, M. (2010). An elastic plate model for interseismic deformation in subduction zones. *J. Geophys. Res.*, 115:B03405.

Khazaradze, G. and Klotz, J. (2003). Short- and long-term effects of GPS measured crustal deformation rates along the south central Andes. *J. Geophys. Res.*, 108:2289.

King, R. W. and Bock, Y. (2002). *Documentation for the GAMIT Analysis Software release10.0*. Mass, Inst. of Technol., Cambridge.

Kley, J. and Monaldi, C. R. (1998). Tectonic shortening and crustal thickness in the central andes: How good is the correlation? *Geology*, 26(8):723–726.

Klotz, J., Angermann, D., Michel, G. W., Porth, R., Reigber, C., Reinking, J., Viramonte, J., Perdomo, R., Rios, V. H., Barrientos, S., Barriga, R., and Cifuentes, O. (1999). GPS-derived Deformation of the Central Andes Including the 1995 Antofagasta Mw = 8.0 Earthquake. *Pure Appl. Geophys.*, 154:709–730.

Langbein, J. and Johnson, H. (1997). Correlated errors in geodetic time series: Implications for time-dependent deformation. *J. Geophys. Res.*, 102(B1):591–603.

Mao, A., Harrison, C. G. A., and Dixon, T. H. (1999). Noise in GPS coordinate time series. *J. Geophys. Res.*, 104(B2):2797–2816.

Massonnet, D. and Feigl, K. L. (1998). Radar interferometry and its application to changes in the earth's surface. *Rev. Geophys.*, 36:441–500.

Menke, W. (1989). *Geophysical Data Analysis: Discrete Inverse Theory, Rev. ed.* Academic Press, New York.

Norabuena, E., Leffler-Griffin, L., Mao, A., Dixon, T., Stein, S., Selwyn Sacks, I., Ocola, L., and Ellis, M. (1998). Space Geodetic Observations of Nazca-South America Convergence Across the Central Andes. *Science*, 279(5349):358–362.

Norabuena, E. O., Dixon, T. H., Stein, S., and Harrison, C. G. A. (1999). Decelerating Nazca-South America and Nazca-Pacific plate motions. *Geophys. Res. Lett.*, 26:3405–3408.

Okada, Y. (1985). Surface deformation due to shear and tensile faults in a half- space. *Bull. Seismol. Soc. Am.*, 75:1135–1154.

Peyrat, S., Campos, J., de Chabalier, J. B., Perez, A., Bonvalot, S., Bouin, M., Legrand, D., Nercessian, A., Charade, O., Patau, G., Clevede, E., Kausel, E., Bernard, P., and Vilotte, J. (2006). Tarapaca intermediate-depth earthquake (Mw 7.7, 2005, northern Chile): A slab-pull event with horizontal fault plane constrained from seismologic and geodetic observations. *Geophys. Res. Lett.*, 33:L22308.

Remy, D., Falvey, M., Bonvalot, S., Chlieh, M., Gabalda, G., Froger, J. L., and Legrand, D. (2011). Variability of atmospheric precipitable water in northern Chile: Impacts on interpretation of InSAR data for earthquake modeling. *J. S. Am. Earth. Sci.*, 31(2-3):214–226.

Rosen, P. A., Henley, S., Peltzer, G., and Simons, M. (2004). Updated Repeat Orbit Interferometry Package Released. *EOS Transactions*, 85(5):47.

Savage, J. C. (1983). A dislocation model of strain accumulation and release at a subduction zone. *J. Geophys. Res.*, 88:4984–4996.

Sella, G. F., Dixon, T. H., and Mao, A. (2002). REVEL: A model for Recent plate velocities from space geodesy. *J. Geophys. Res.*, 107:2081.

Vigny, C., Rudloff, A., Ruegg, J., Madariaga, R., Campos, J., and Alvarez, M. (2009). Upper plate deformation measured by GPS in the Coquimbo Gap, Chile. *Phys. Earth Planet. Int.*, 175:86–95.